High Energy Emission from Pulsar Magnetospheres

Kouichi HIROTANI

ASIAA/TIARA-NTHU, Taiwan

Workshop on BH Magnetospheres
March 1, 2012

Crab nebula: Composite image of X-ray [blue] and optical [red]

§1 γ-ray Pulsar Observations

Fermi/LAT has detected more than 121 pulsars above 100 MeV.

Large Area Telescope

Fermi γ-ray space telescope

Fermi/LAT point sources (>100 MeV)

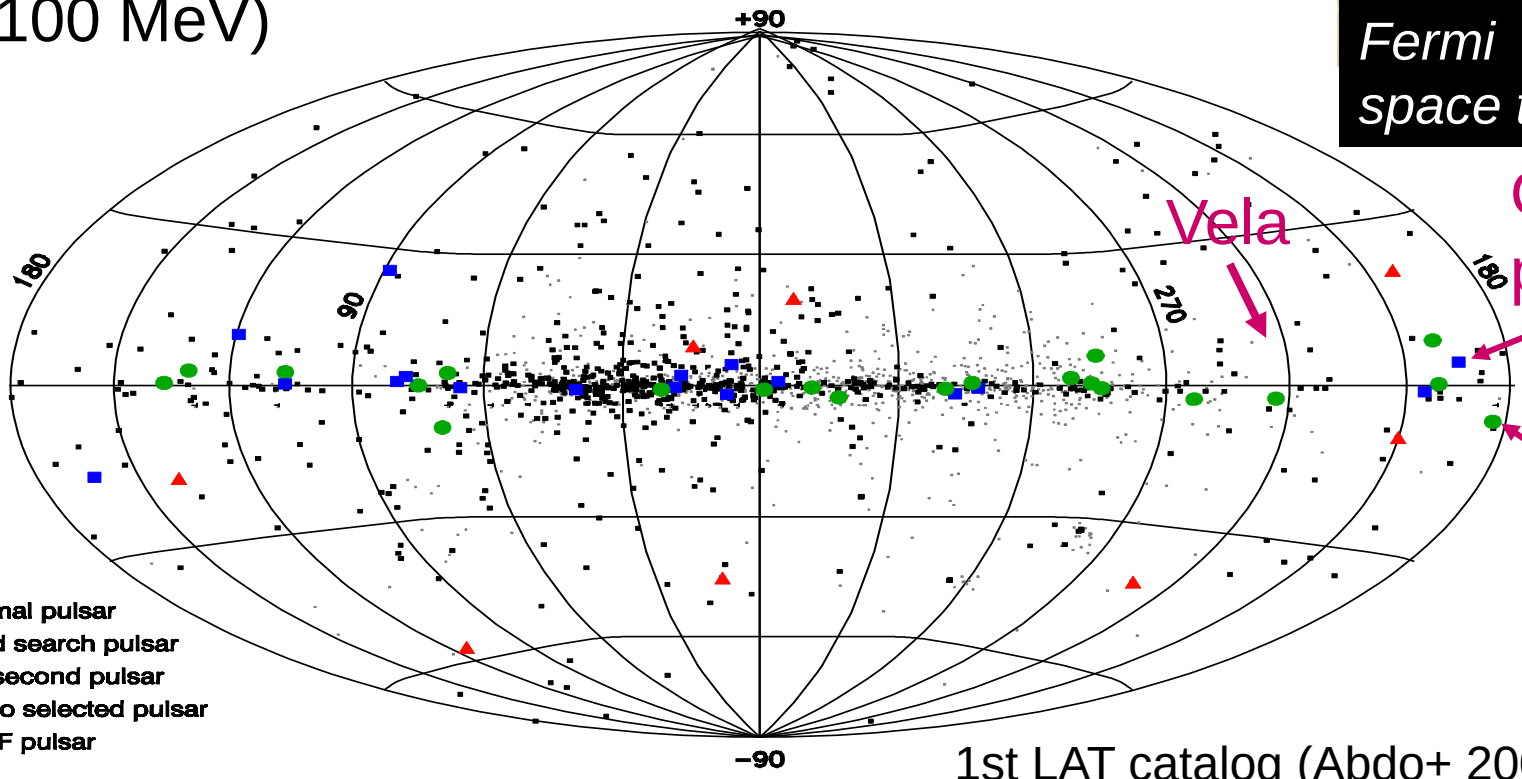

Vela

Geminga pulsar

Crab pulsar

1st LAT catalog (Abdo+ 2009)

§1 γ-ray Pulsar Observations

Recent IACTs found pulsed emission in 25-400 GeV from the Crab pulsar.

VERITAS (> 120 GeV)

Aliu+ (2011, Science 334, 69)

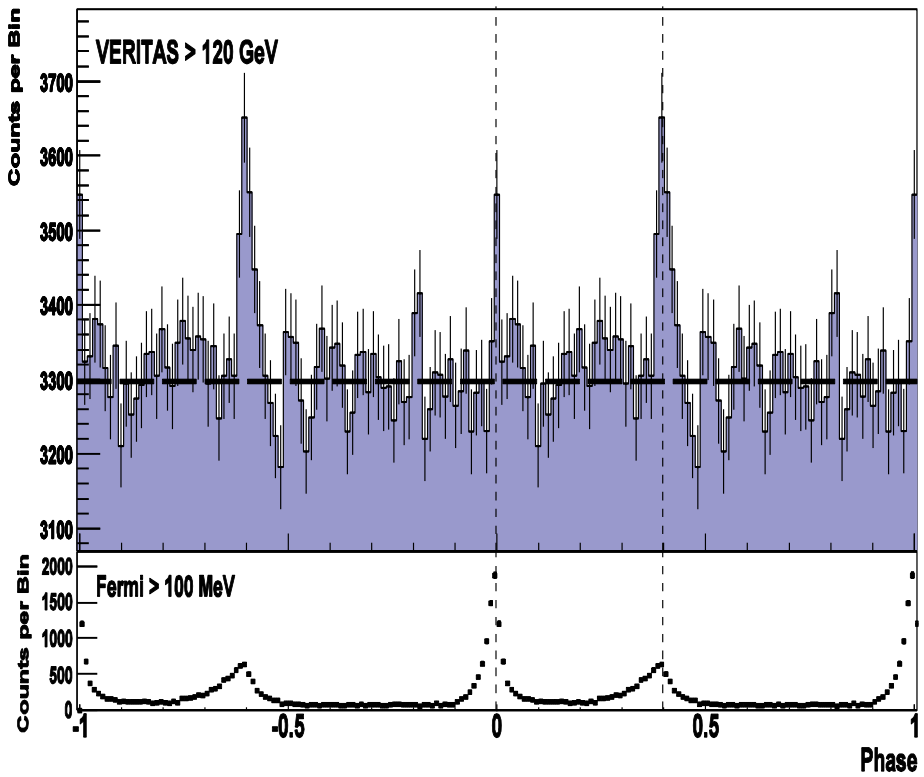

MAGIC (25–416 GeV)

Aleksić+ (2011a,b)

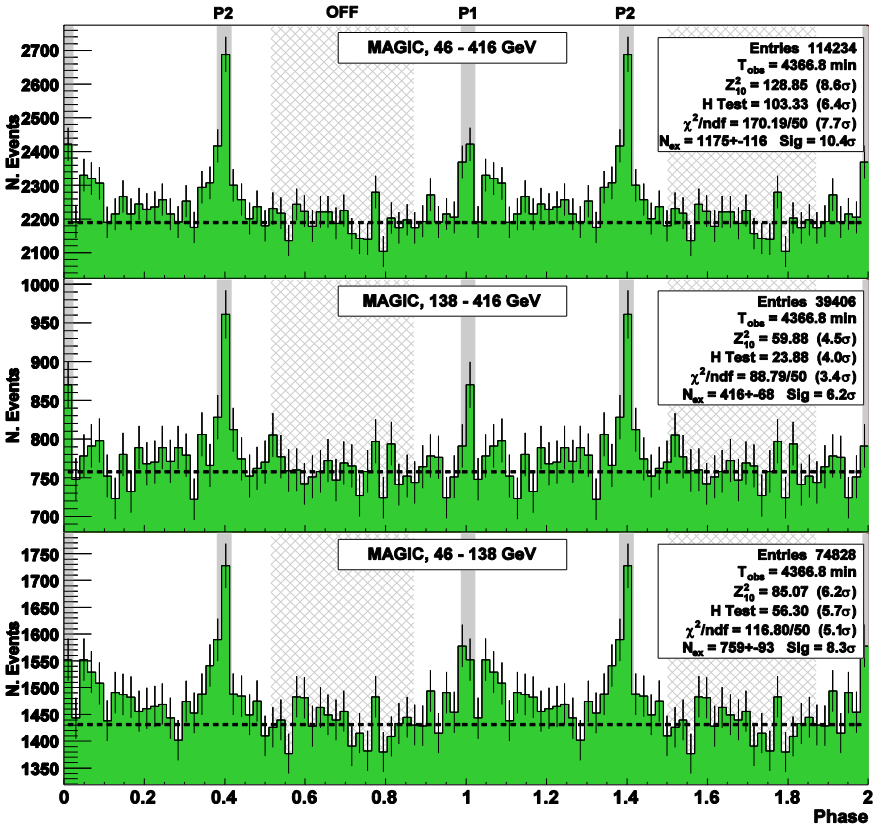

§1 Introduction

L_{spin} ($< 10^{39}$ erg s^{-1}) is dissipated at …

- Inner magnetosphere

  (r ~30 km)

  close to the NS surface

- Outer magnetosphere

  (r ~1000 km)

  near the 'light cylinder'

- Wind region

  ($r \sim 10^{-1\sim0}$pc)

  in the inter-stellar medium

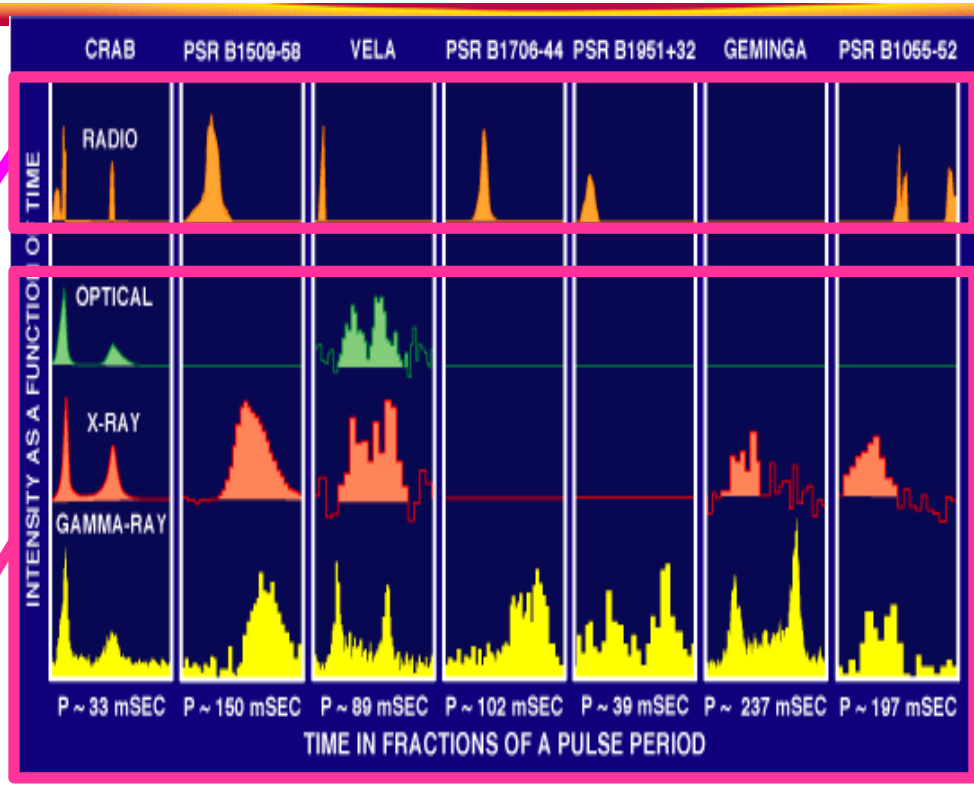

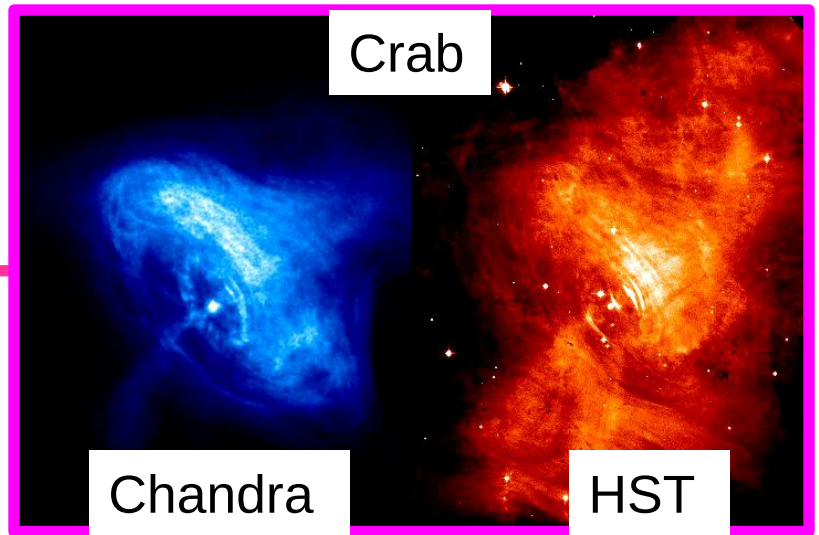

§1 Introduction

L_{spin} ($< 10^{39}$ erg s^{-1}) is dissipated at …

- Inner magnetosphere ~ 0.001%
  (r ~30 km) → pulsed radio

  $E_{||}$ arises along ***B*** in a limited volume near the PC surface.

- Outer magnetosphere 0.1−20%
  (r ~1000 km) → pulsed X, γ-ray

  $E_{||}$ is screened much less efficiently.

- Wind region 80−99.9%
  (r ~ $10^{-1\sim0}$pc) → PWN emission

§1 Introduction

L_{spin} ($< 10^{39}$ erg s^{-1}) is dissipated at …

- Inner magnetosphere ~ 0.001%
  (r ~30 km) → pulsed radio
- Outer magnetosphere 0.1–20%
  (r ~1000 km) → pulsed X, γ-ray
- Wind region 80–99.9% (slightly outside the LC)
  (r ~ pc) → PWN emission

Pulsed emissions

§1 Introduction

Today, I compare several representative models and consider a quantitative extension of the OG model in detail.

- Inner magnetosphere ~ 0.001% Polar-cap (PC) model
  (r ~30 km) → pulsed radio
- Outer magnetosphere 0.1−20% Outer-gap (OG) model
  (r ~1000 km) → pulsed X, γ-ray Slot-gap (SG) model
  Pair-starved PC model
- Wind region 80−99.9%
  ($r \sim 10^{-1\sim0}$pc) → PWN emission

Broad-band spectra (pulsed)

- High-energy (>100MeV) photons are emitted mainly via **curvature** process by ultra-relativistic (~10 TeV) $e^{\pm}$'s accelerated in pulsar magnetosphere.

- Above 20 GeV, **ICS by secondary/tertiary pairs** contributes.

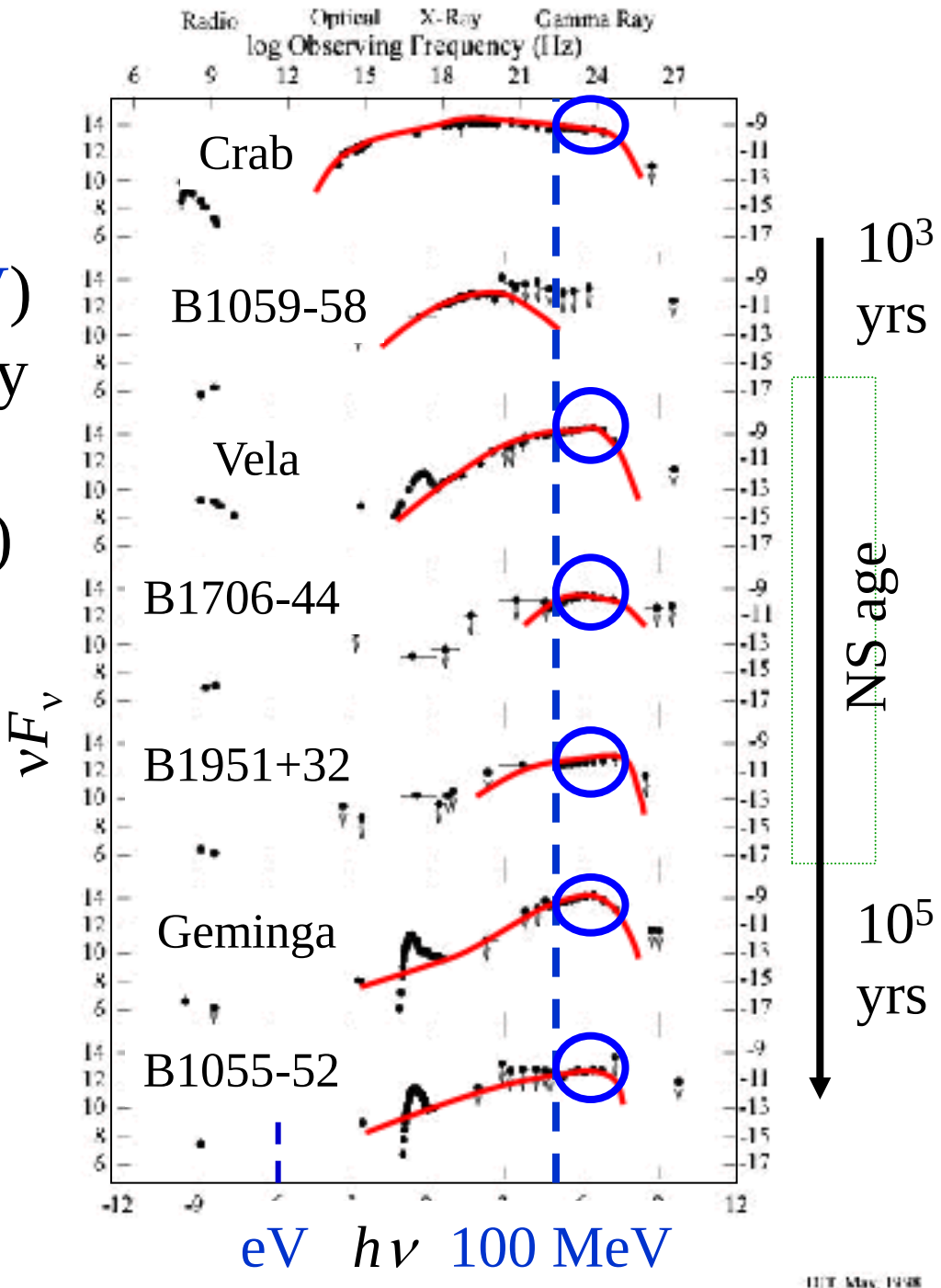

Broad-band spectra (pulsed)

- High-energy (> 100MeV) photons are emitted mainly via **curvature** process by ultra-relativistic (~10 TeV) $e^{\pm}$'s accelerated in pulsar magnetosphere.

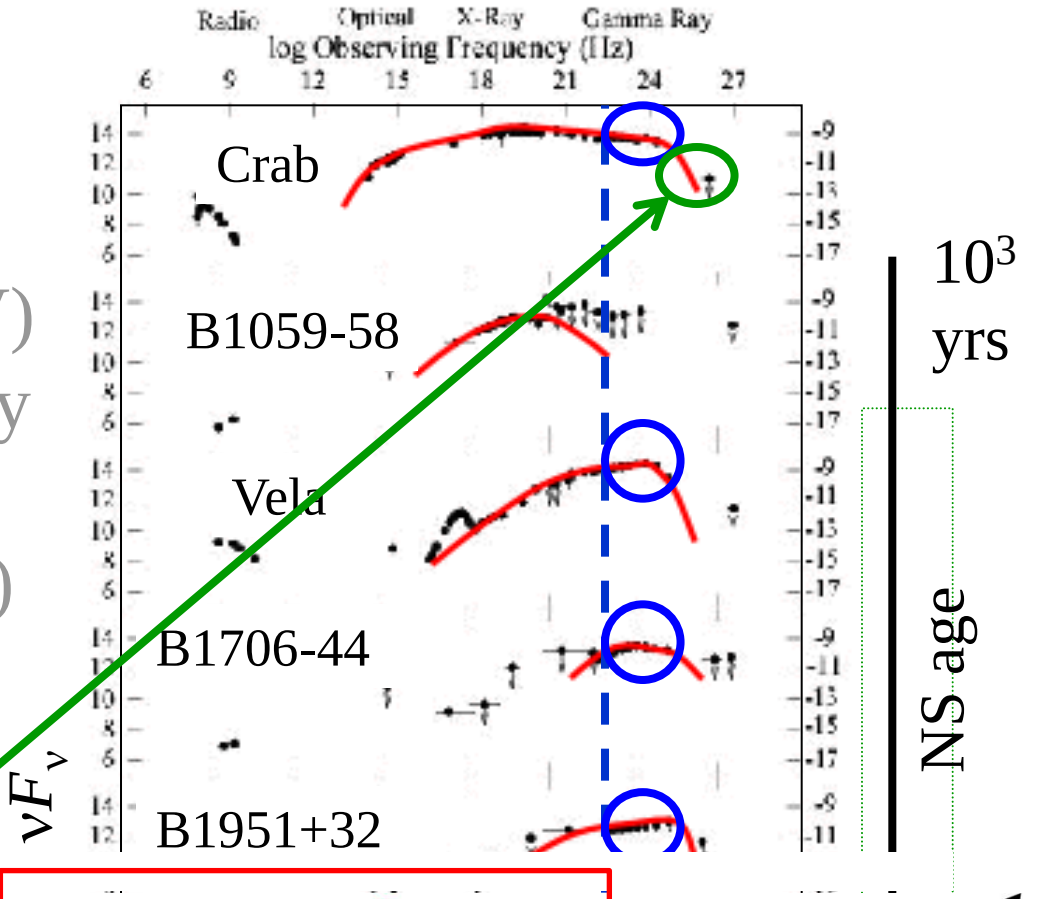

- Above 20 GeV, **ICS by secondary/tertiary pairs** contributes.

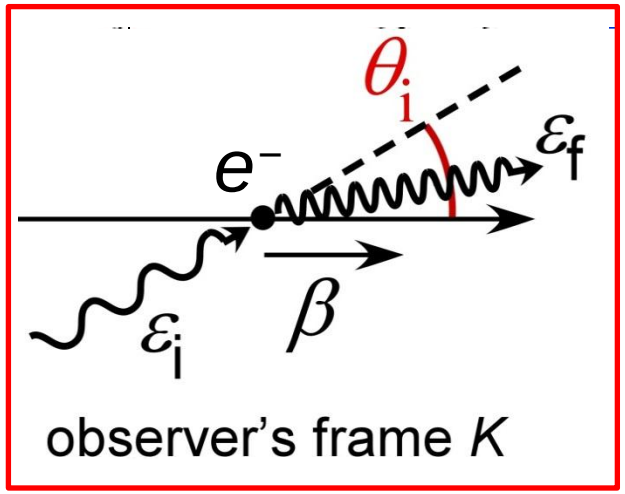

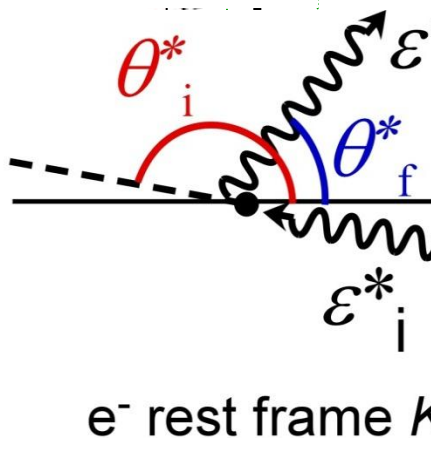

Broad-band spectra (pulsed)

- High-energy (> 100MeV) photons are emitted mainly via **curvature** process by ultra-relativistic (~10 TeV) $e^{\pm}$'s accelerated in pulsar magnetosphere.

- Some of the **primary** γ-rays are absorbed in the NS magnetosphere and reprocessed in lower energies via **synchrotron** process.

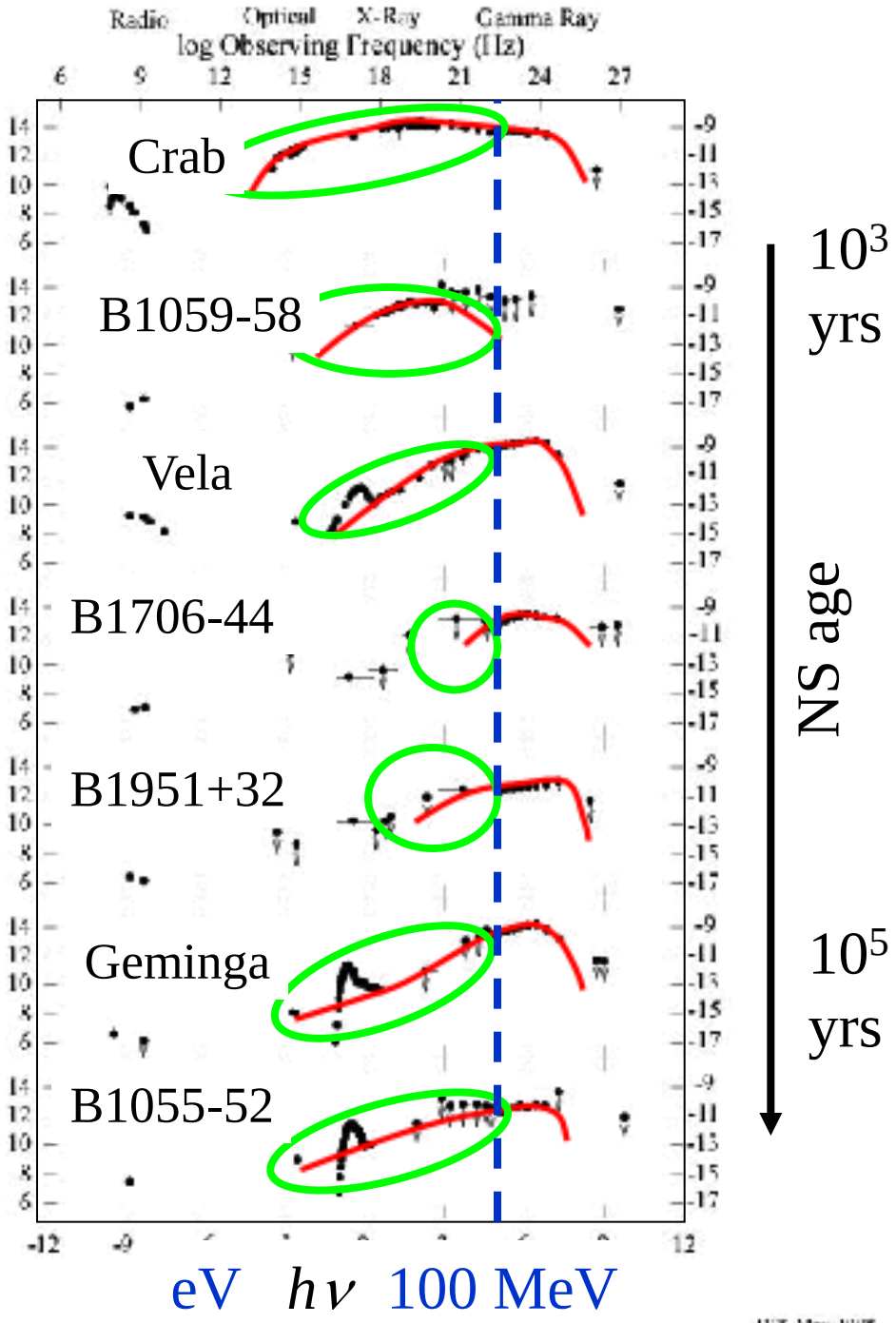

§1 Introduction

Such high-energy emissions are realized when the rotational energy of the NS is electro-dynamically extracted and partly dissipated in the inner and/or outer magnetosphere.

(e.g., unipolar inductor)

§2 Rotating NS Magnetosphere

Pulsars:

rapidly rotating, highly magnetized neutrons stars (NS)

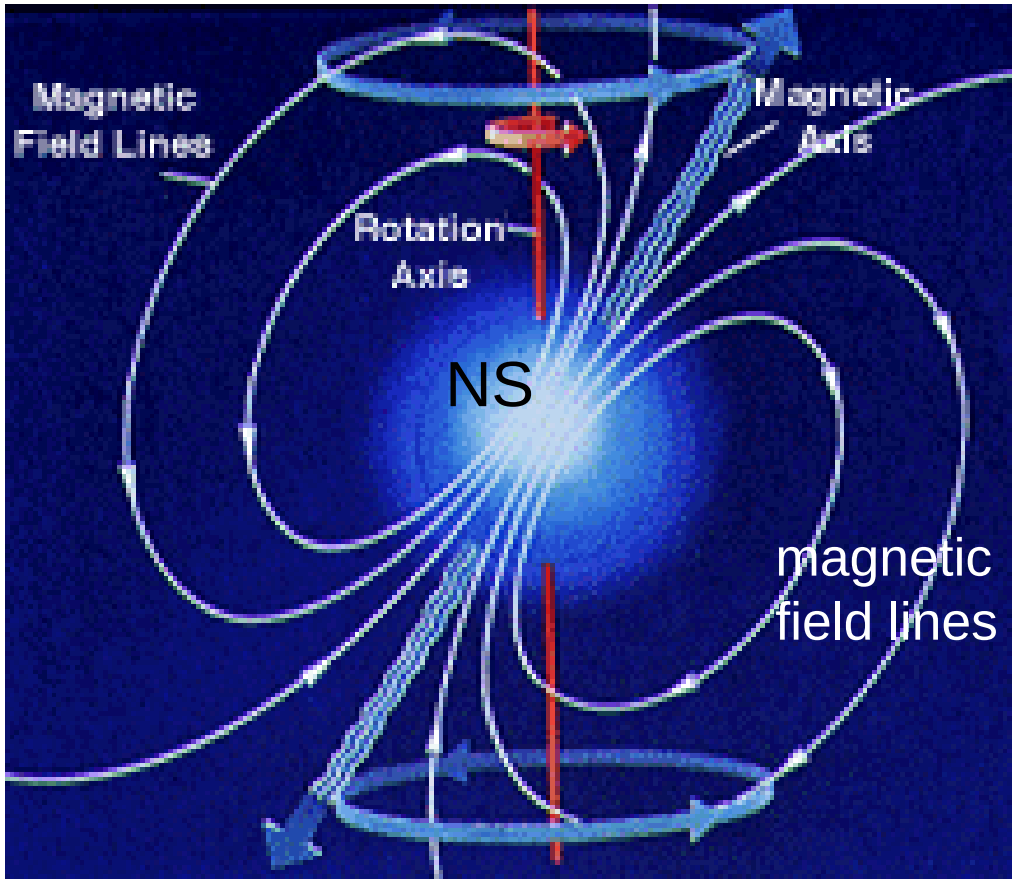

Magnetic and rotation axes are misaligned.

Pulsar turns on and off as the beam sweeps our line of sight (e.g., lighthouse).

§2 Rotating NS Magnetosphere

A rotating NS magnetosphere can be divided into open and closed zones.

Last-open field lines form the boundary of them.

In the open zone, $e^{\pm}$'s escape through the light cylinder as a pulsar wind.

In the closed zone, on the other hand, an $E_{\parallel}$ would be very quickly screened by the dense plasmas.

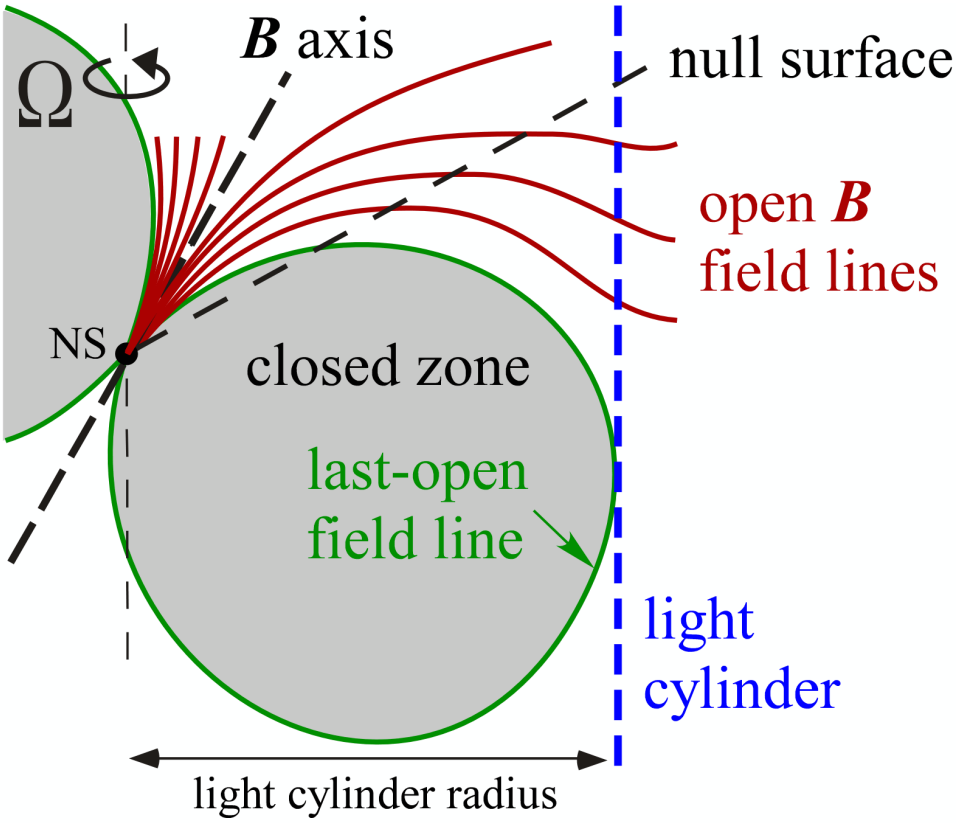

$$\varpi_{LC} = 3\times10^{8}(\Omega/10^{2}\,\mathrm{rad\,s^{-1}})\ \mathrm{cm}$$

§2 Rotating NS Magnetosphere

A rotating NS magnetosphere can be divided into open and closed zones.

Last-open field lines form the boundary of them.

In the open zone, $e^{\pm}$'s escape through the light cylinder as a pulsar wind.

In the closed zone, on the other hand, an $E_{\parallel}$ would be very quickly screened by the dense plasmas.

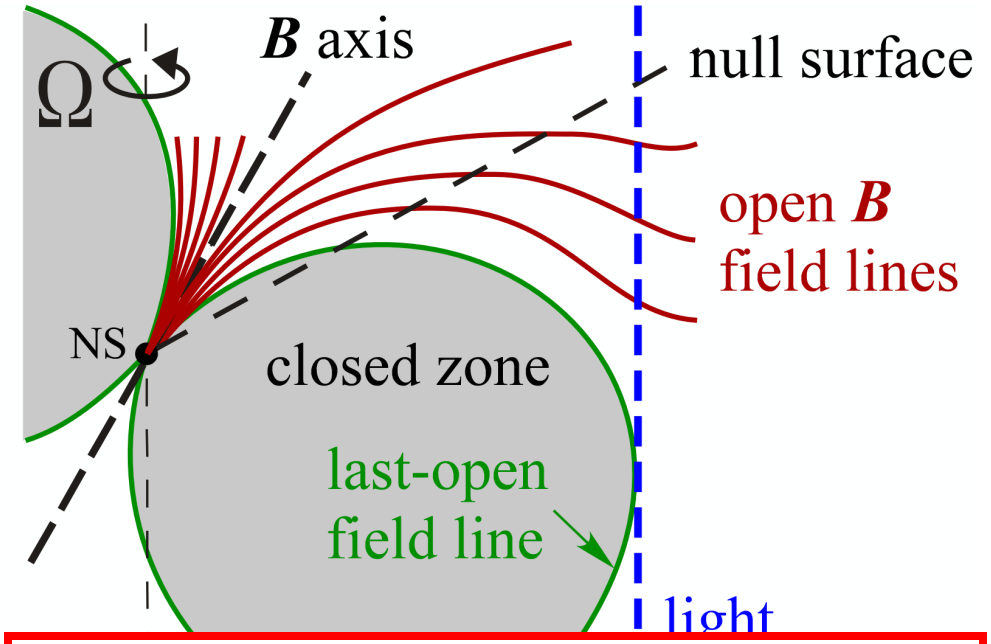

Thus, in all pulsar emission models, particle acceleration takes place only within the open zone.

§2 Rotating NS Magnetosphere

For typical high-energy pulsars, open zone occupies only a few degrees from ***B*** axis on the PC surface.

Available voltage in the open zone:

$$\mathrm{EMF} \sim \frac{\Omega^2 B_* r_*^3}{c^2} \sim 10^{15.5}\ \mathrm{V}$$

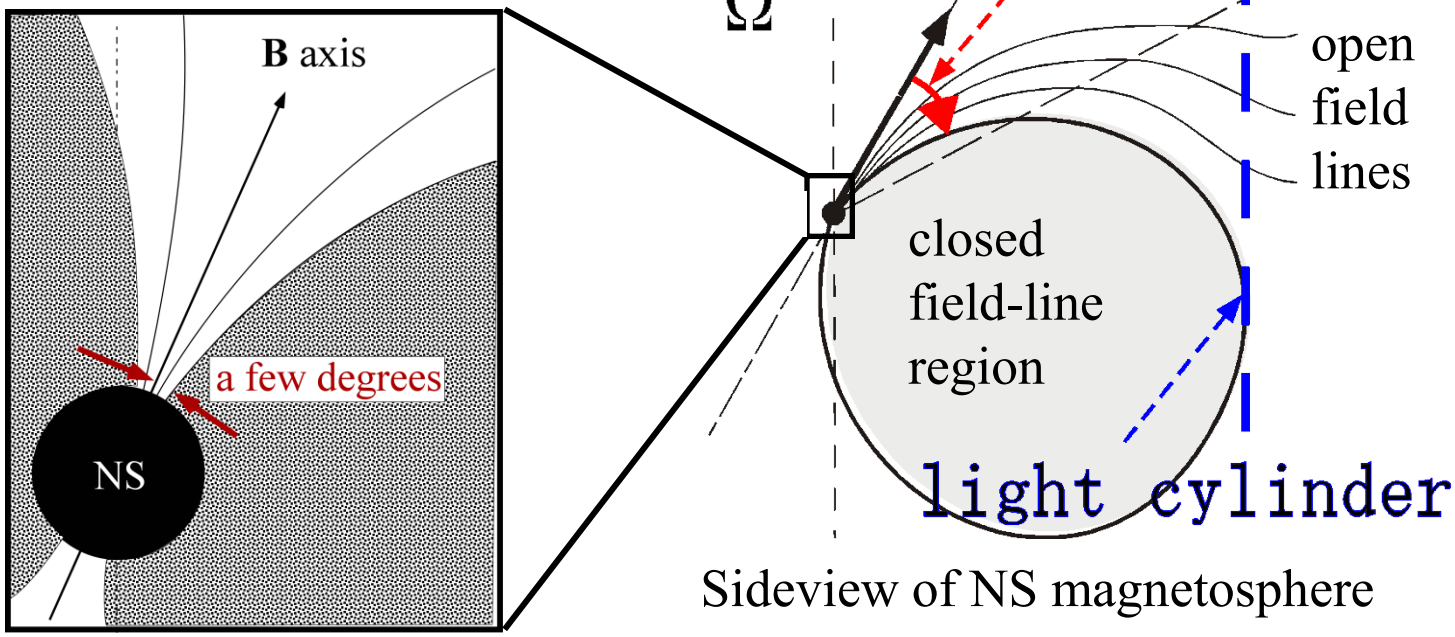

Sideview of NS magnetosphere

§2 Rotating NS Magnetosphere

In a rotating NS magnetosphere, the Goldreich-Julian charge density is induced for a static observer. The inhomogeneous part of Maxwell eqs. give

$$\nabla \cdot \mathbf{E}_{\parallel} = 4\pi(\rho - \rho_{\mathrm{GJ}}),$$

where $E_{\parallel} \equiv \mathbf{E}\bullet\mathbf{B}$, $\rho \equiv e(n_{+} - n_{-})$ and

$$\rho_{\mathrm{GJ}} \equiv \frac{1}{4\pi}\nabla \cdot \mathbf{E}_{\perp} = -\frac{\boldsymbol{\Omega}\cdot\mathbf{B}}{2\pi c}.$$

Thus, $E_{\parallel}$ arises if $\rho \neq \rho_{\mathrm{GJ}}$.

Note that ρ_{GJ} is uniquely determined by ***B***-field geometry. For example, it changes sign at the so-called 'null-charge surface'.

§2 Rotating NS Magnetosphere

Note that $\rho_{\rm GJ}$ is uniquely determined by ***B***-field geometry. For example, it changes sign at the so-called 'null-charge surface'.

$$\rho_{\rm GJ} \equiv \frac{1}{4\pi}\nabla\cdot\mathbf{E}_{\perp}$$
$$= -\frac{\mathbf{\Omega}\cdot\mathbf{B}}{2\pi c}.$$

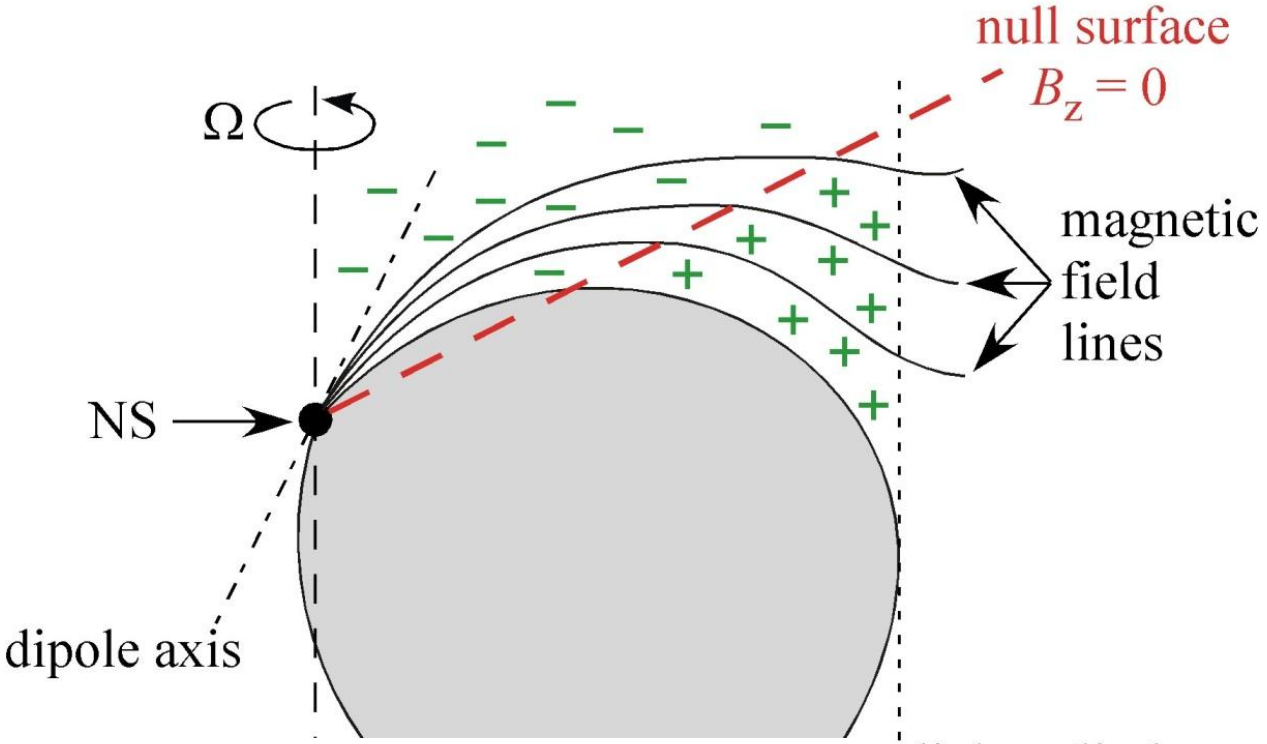

$$\rho_{\rm GJ} \equiv \frac{c^2}{4\pi\sqrt{-g}}\partial_\mu\left[\frac{\sqrt{-g}}{\rho_{\rm w}^{\,2}}\,g^{\mu\nu}g_{\phi\phi}\left(\Omega_{\rm F}-\omega\right)F_{\phi\nu}\right]$$

§3 Traditional Emission Models

Next question:

Where is the particle accelerator, in which $\boldsymbol{E}_{\parallel}$ arises?

In this section, we geometrically consider three representative pulsar high-energy emission models:

(historical order)

1. Inner-gap (or polar-cap) model, 1982-1990's
2. Outer-gap model, 1986-present
3. Slot-gap model 2003-2009

Note: Polar-cap model still survives as a phenomenological model of coherent radio emissions.

§3 Traditional Emission Models

Schematic view of the three representative emission models:

- **polar gap (inner gap)**
  (Daugherty & Harding 1996 ApJ 458, 278)
- **slot gap**
  (Arons 1983, ApJ 302, 301; Muslimov & Harding 2004, ApJ 606, 1143)
- **outer gap**
  (Cheng, Ho, Ruderman 1986, ApJ 300, 500)

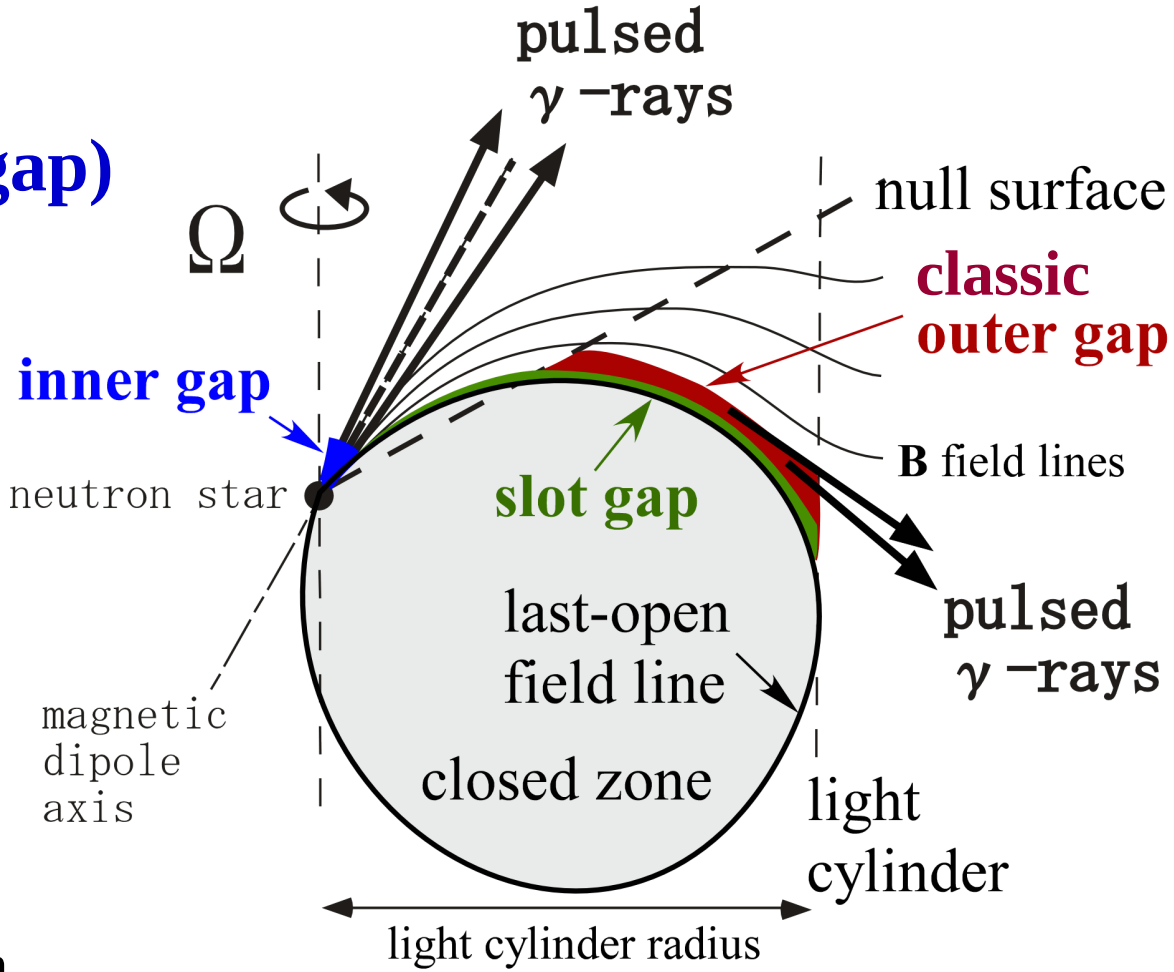

§3 Traditional Emission Models

Early 80's, the polar-cap (PC) model was proposed.

(Daugherty & Harding ApJ 252, 337, 1982)

Emission altitude < $3r_{NS}$ ⟶ pencil beam ($\Delta\Omega$ «1 ster)

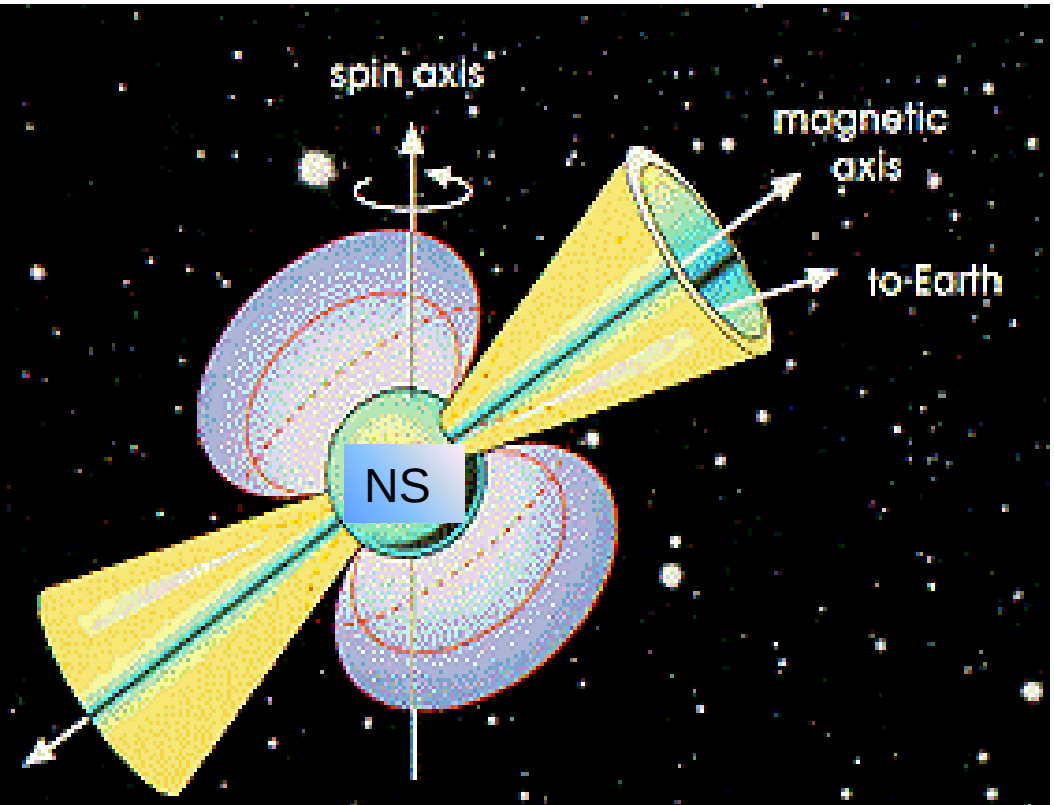

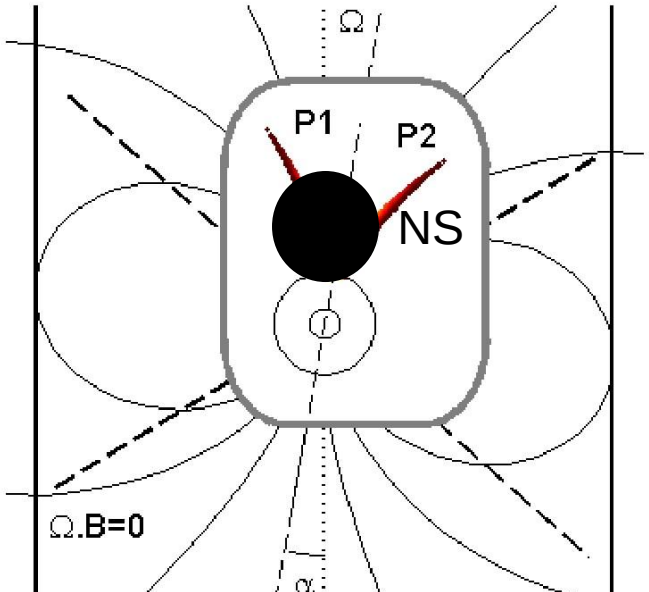

§3 Traditional Emission Models

Early 80's, the polar-cap (PC) model was proposed.

(Daugherty & Harding ApJ 252, 337, 1982)

Emission altitude < $3r_{NS}$ ⟶ pencil beam ($\Delta\Omega$ «1 ster)

Difficult to explain wide-separated double peaks (in X-ray, γ-ray)

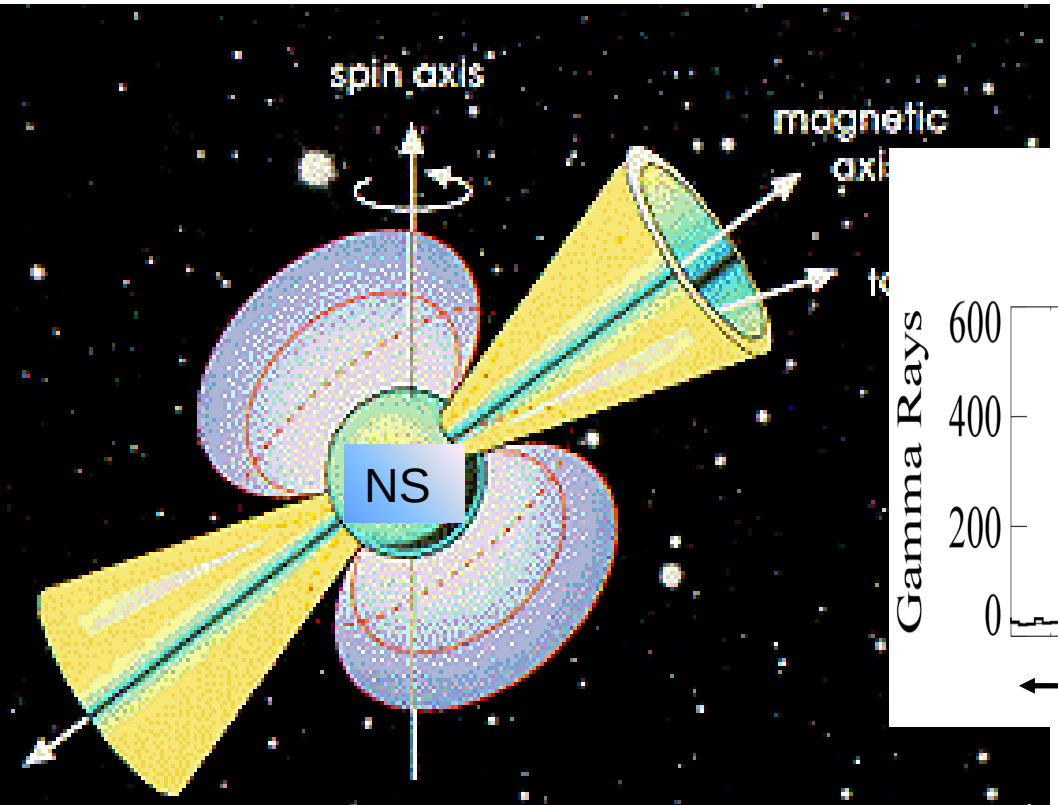

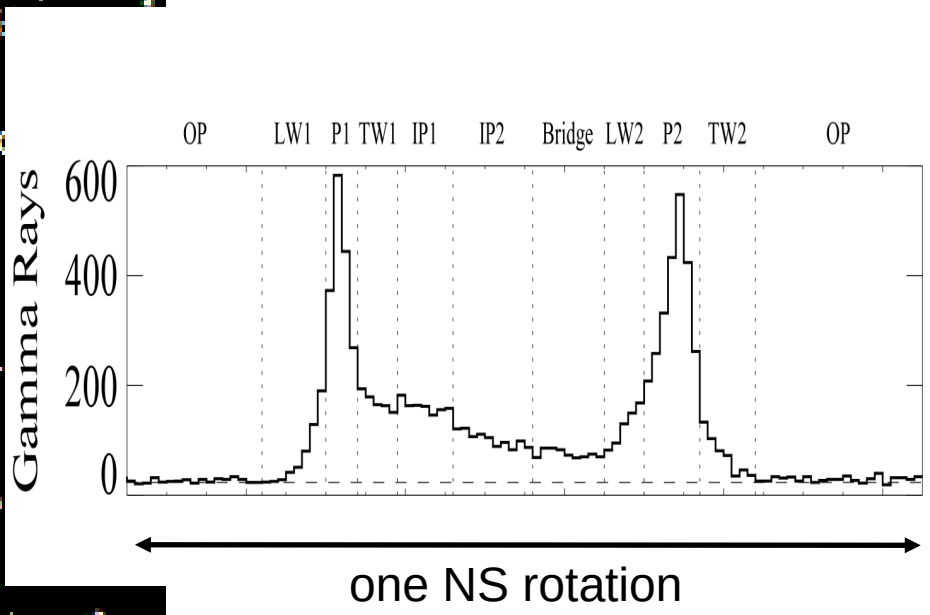

§3 Traditional Emission Models

Early 80's, the polar-cap (PC) model was proposed.

(Daugherty & Harding ApJ 252, 337, 1982)

Emission altitude $< 3r_{NS}$ ⟶ pencil beam ($\Delta\Omega$ «1 ster)

Difficult to explain wide-separated double peaks (in X-ray, γ-ray)

Thus, a high-altitude emission model drew attention.

§3 Traditional Emission Models

Mid 80's, the outer-gap (OG) model was proposed.

(Cheng, Ho, Ruderman ApJ 300, 500, 1986)

Emission altitude > 100 r_{NS} ⟶ hollow cone emission ($\Delta\Omega > 1$ ster)

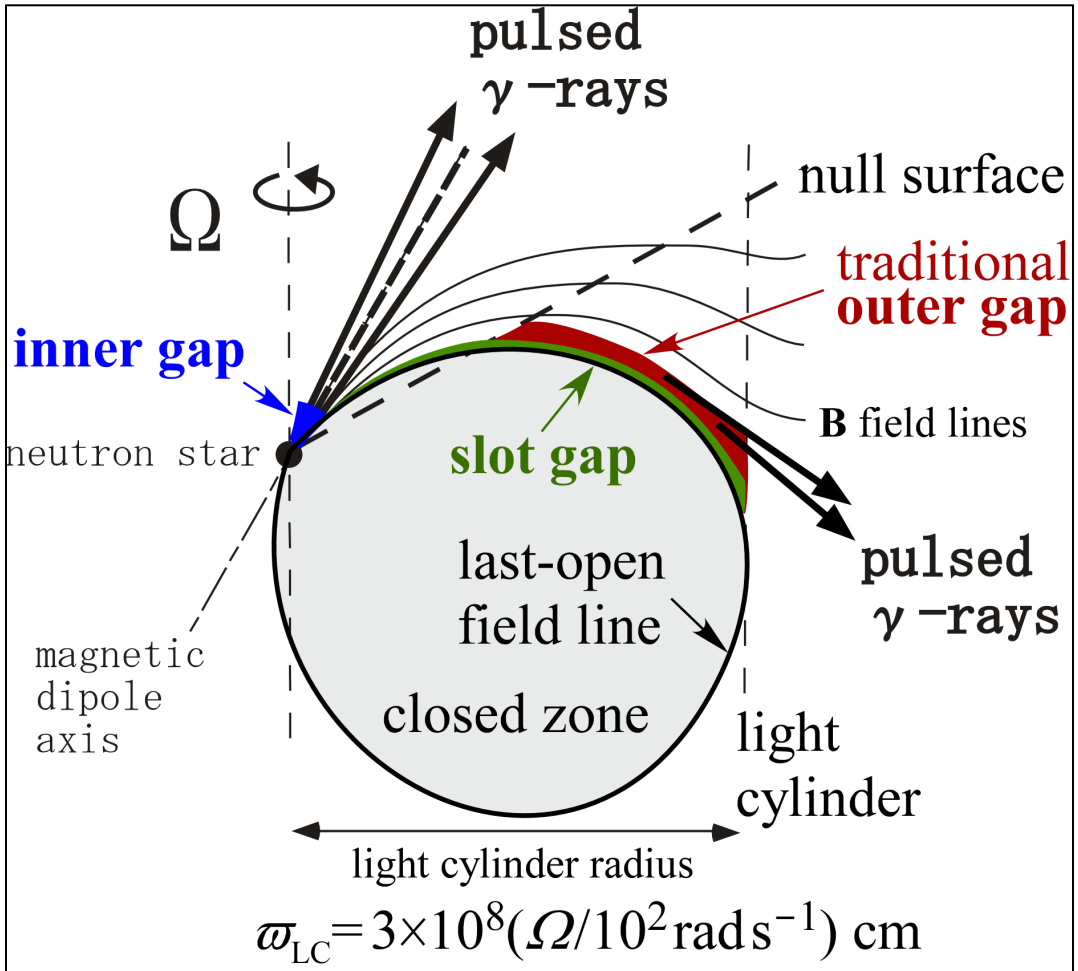

§3 Traditional Emission Models

Mid 80's, the outer-gap (OG) model was proposed.

(Cheng, Ho, Ruderman ApJ 300, 500, 1986)

Emission altitude > 100 r_{NS} ⟶ hollow cone emission ($\Delta\Omega > 1$ ster)

Mid 90s', the outer-gap model was further developed by taking account of special relativistic effects.

(Romani ApJ 470, 469)

⟶ Explains wide-separated double peaks.

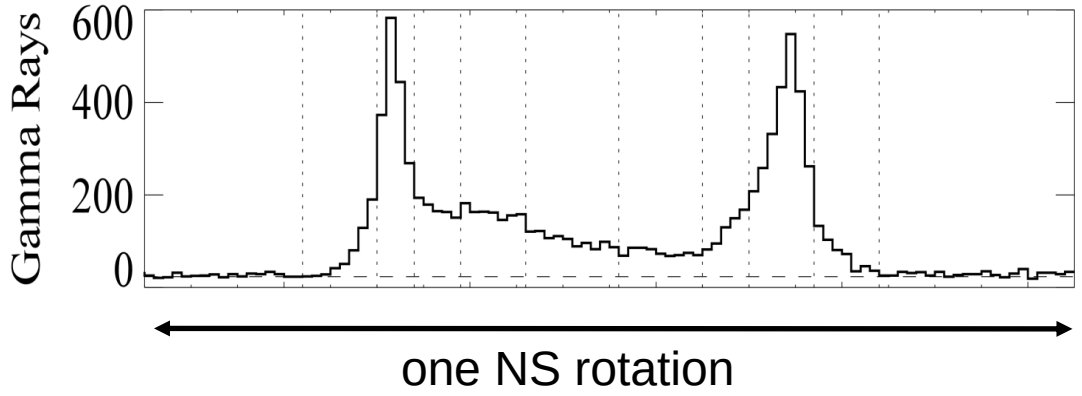

§3 Traditional Emission Models

Special relativistic effects in outer magnetosphere:

On the leading side, phase shifts add up to spread photons emitted at various altitudes over 140^o in phase.

On the trailing side, photons emitted earlier at lower altitudes catch up with those emitted later at higher altitudes to focus in a small phase range 30^o, forming caustics (strong intensity) in the phase plot.

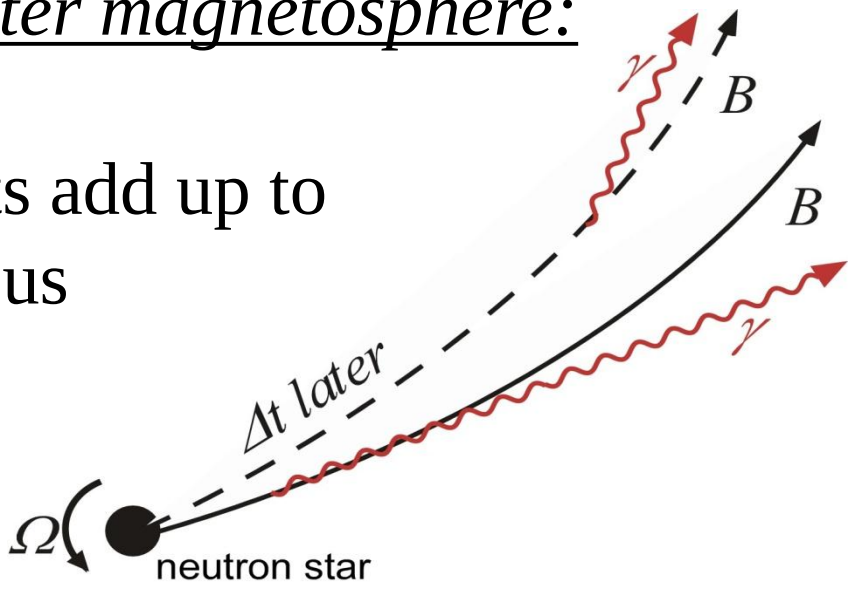

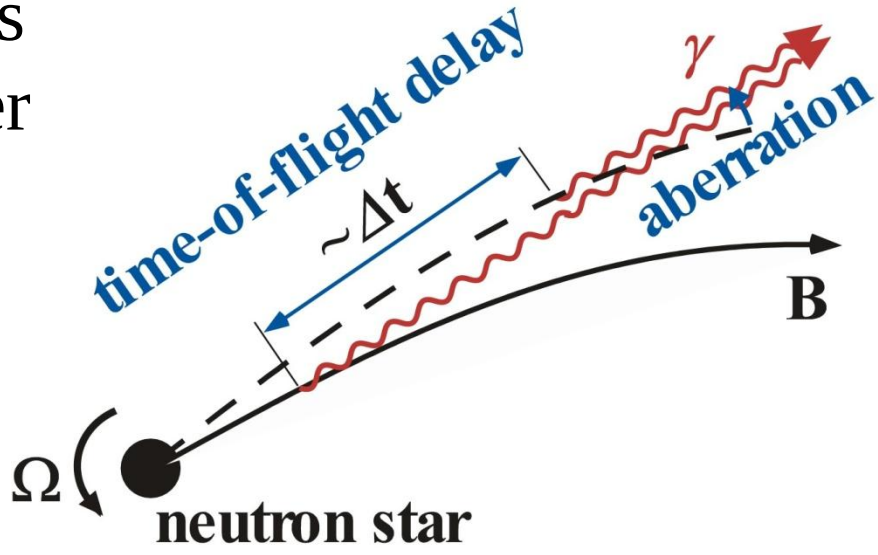

§3 Traditional Emission Models

Mid 80's, outer-gap model was proposed.

(Cheng, Ho, Ruderman ApJ 300, 500, 1986)

Emission altitude > 100 r_{NS} ⟶ hollow cone emission ($\Delta\Omega > 1$ ster)

Mid 90s', the outer-gap model was further developed by taking account of special relativistic effects.

(Romani ApJ 470, 469)

⟶ Explains wide-separated double peaks.

Outer-gap model became promising.

§3 Traditional Emission Models

Early 00's, an alternative mode, slot-gap model, was proposed. (Muslimov & Harding ApJ 588, 430, 2003)

They revisited the original idea of Arons (1983), extending his lower-altitude slot-gap model into the higher altitudes (by hand).

Due to special relativistic effects, wide-separated double peaks also appear, in the same way as in the outer-gap model (although the peak formation mechanism is slightly different).

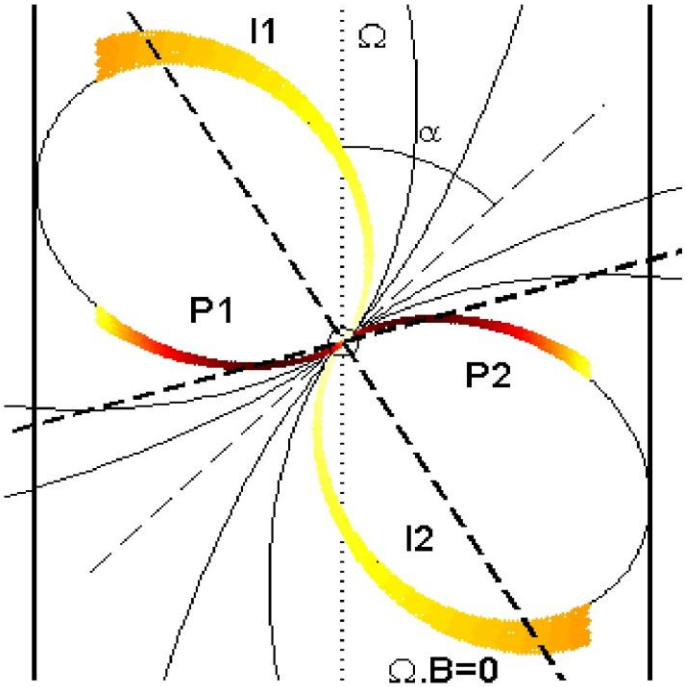

§3 Traditional Emission Models

However, a SG, which is geometrically thin, cannot reproduce the observed γ-ray fluxes.

In the Crab pulsar (Ω=190 rad s^{-1}):

KH (2008) ApJ 688, L25

For OG model (f~0.14, κ~0.3, $\mu=4\times10^{30}$ G cm^3),

$$(\nu F_\nu)_{\rm peak} \sim 4\times10^{-4}\ {\rm MeV\ s^{-1}\ cm^{-2}} \sim {\rm Fermi\ flux}.$$

For SG model (f~0.04, κ~0.2, large μ),

$$(\nu F_\nu)_{\rm peak} \sim 3\times10^{-5}\,(\mu/8\times10^{30})^2\ {\rm MeV\ s^{-1}\ cm^{-2}} < 0.1\ {\rm Fermi\ flux}.$$

For other pulsars, the thin SG model predicts further smaller fluxes than (typically < 1% of) observed.

§3 Traditional Emission Models

However, a SG, which is geometrically thin, cannot reproduce the observed γ-ray fluxes.

In fact, classic thin OG model has the same difficulty.

On these grounds, all the pulsar emission models adopt transversely thick accelerator geometry.

occupying a good fraction of open zone

§3 Traditional Emission Models

To contrive a geometrically thick gap, the pair-starved PC (PSPC) model was proposed (Venter + 2009 ApJ 707, 800).

Large $e^{\pm}$ production (by extracted e^{-}'s) → SG

Medium $e^{\pm}$ production (by self-sustained $e^{\pm}$'s) → OG

Small $e^{\pm}$ production (by extracted e^{-}'s) → PSPC

Both OG and PSPC models can produced the observed γ-ray fluxes.

§3 Traditional Emission Models

Two major high-energy emission models:

Outer-gap model	Pair-starved PC model
Arise because of pair starvation in outer **B**-sphere.	Arise because of pair starvation near NS surface.
Pairs produced by $\gamma\gamma \rightarrow ee$ and discharge by $E_{\parallel}>0$.	e^-'s extracted from NS surface by $E_{\parallel}<0$.
e^+'s accelerated outwards.	e^-'s accelerated outwards.

However, there is a serious electro-dynamical inconsistency in the PSPC model

(KH 2011, in HE emission from PSRs and their systems, p. 117).

§5 Difficulties in SG Model: Unphysical GJ Charge

To prevent a sign reversal of $E_{\parallel}$, they assumed that the GJ charge density (per $\boldsymbol{B}$ flux) tends to a constant in the higher altitudes

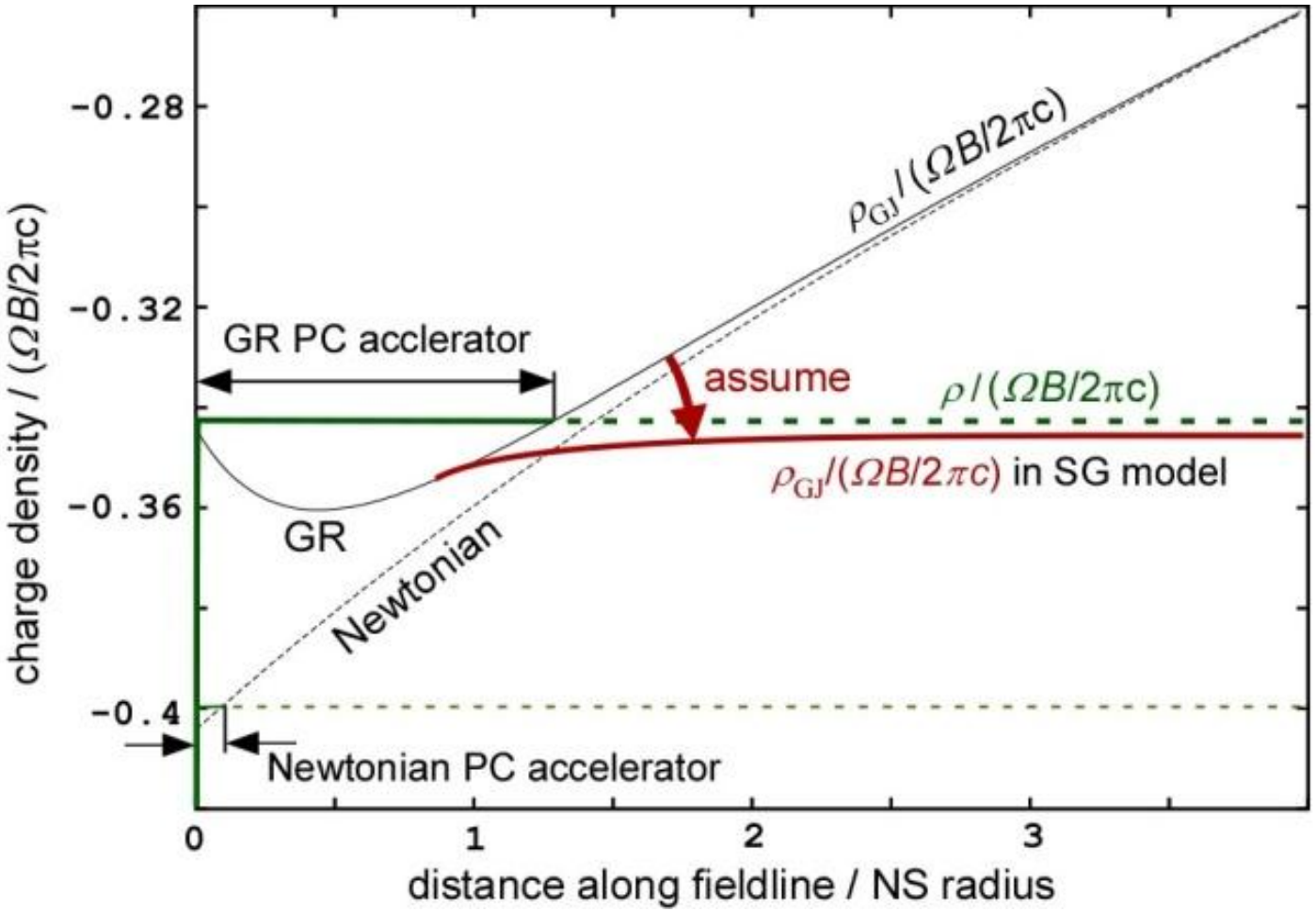

§3 Traditional Emission Models

Two major high-energy emission models:

Outer-gap model	Pair-starved PC model
Arise because of pair starvation in outer **B**-sphere.	Arise because of pair starvation near NS surface.
Pairs produced by $\gamma\gamma \rightarrow ee$ and discharge by $E_{\parallel}>0$.	e^-'s extracted from NS surface by $E_{\parallel}<0$.
e^+'s accelerated outwards.	e^-'s accelerated outwards.

So, we concentrate on the OG emission in this talk.

§3 Traditional Emission Models

Various attempts have been made on recent OG model:

3-D geometrical model

→ phase-resolved spectra (Cheng + '00; Tang + '08)

→ atlas of light curves for PC, OG, SG models (Watters + '08)

2-D self-consistent solution (Takata + '06; KH '06)

3-D self-consistent solution

→ phase-resolved spectra, absolute luminosity if we give only P, dP/dt, α, kT ($+\zeta$) (this talk)

In this talk, I'll present the most recent results obtained in my 3-D version of self-consistent OG calculations.

§4 Modern Outer-gap Model

Self-sustained pair-production cascade in a rotating NS magnetosphere:

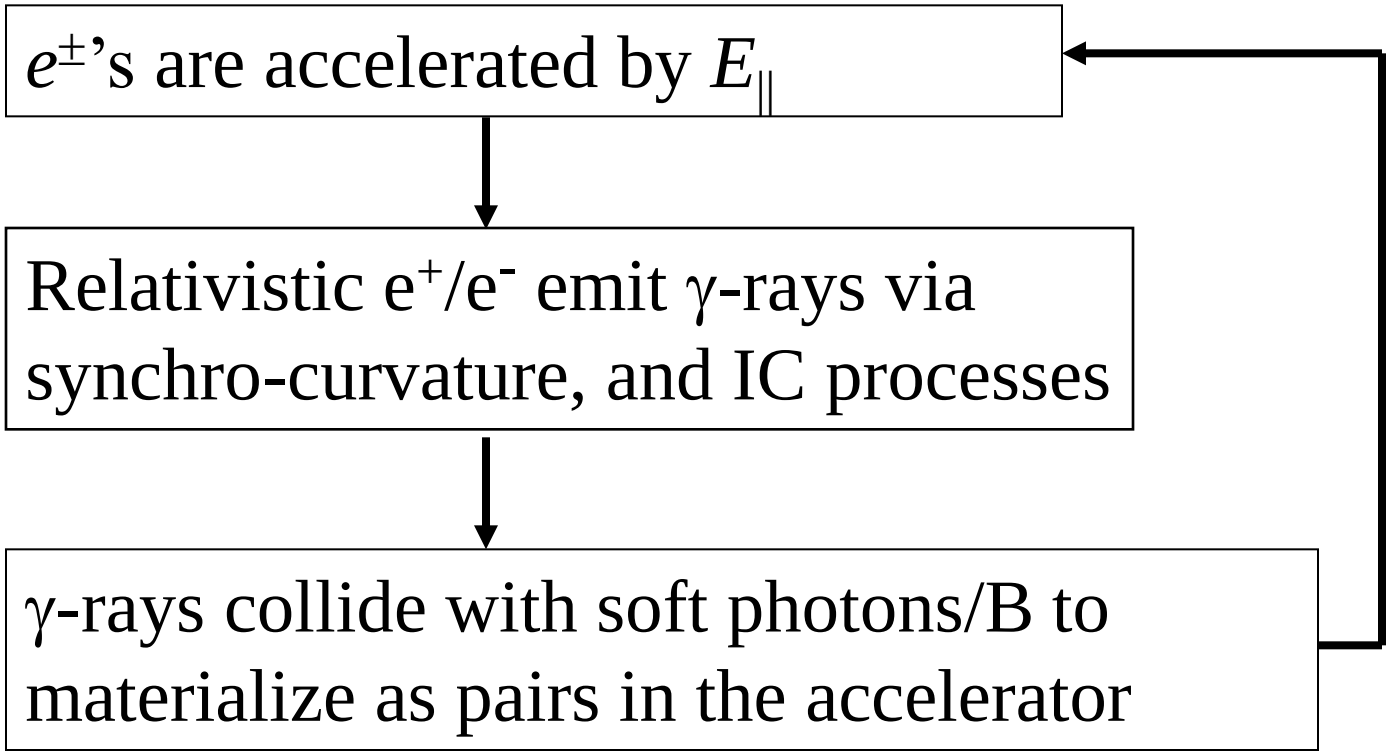

§4 Modern Outer-gap Model

The Poisson equation for the electrostatic potential ψ is given by

$$-\nabla^2\psi = 4\pi(\rho - \rho_{\rm GJ}) \ ,$$

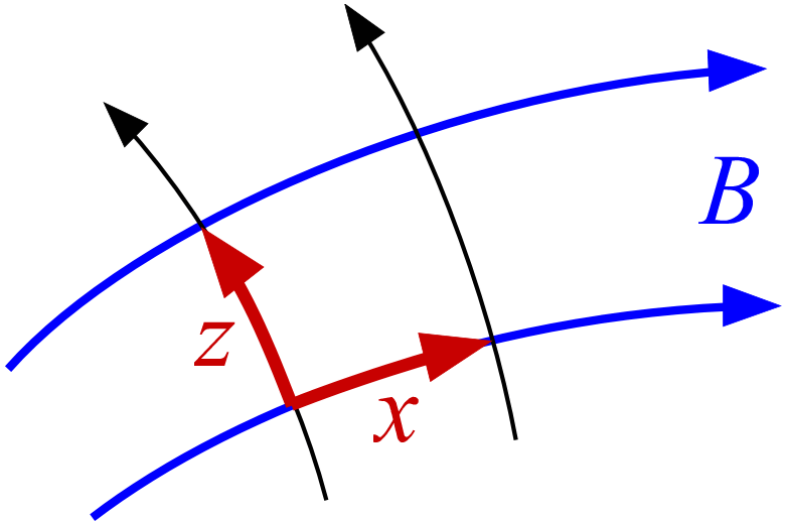

where

$$E_{\parallel} \equiv -\frac{\partial \Psi}{\partial x} \ , \ \rho_{\rm GJ} \equiv -\frac{\mathbf{\Omega \cdot B}}{2\pi c},$$

$$\rho \equiv e\int_0^{\infty} d\mathbf{p}^3 \left[N_+(\mathbf{x},\mathbf{p}) - N_-(\mathbf{x},\mathbf{p}) \right] + \rho_{\rm ion} \ .$$

N_+/N_-: distrib. func. of e^+/e^-

$\boldsymbol{p}$: momentum of e^+/e^-

§4 Modern Outer-gap Model

Assuming $\partial_t+\Omega\partial_\phi=0$, we solve the $e^{\pm}$'s Boltzmann eqs.

$$\frac{\partial N_\pm}{\partial t}+\vec{v}\cdot\nabla N_\pm+\left(e\vec{E}_{\|}+\frac{\vec{v}}{c}\times\vec{B}\right)\cdot\frac{\partial N_\pm}{\partial\vec{p}}=S_{IC}+S_{SC}+\int\alpha_\nu d\nu\int\frac{I_\nu}{h\nu}d\omega$$

together with the radiative transfer equation,

$$\frac{dI_\nu}{dl}=-\alpha_\nu I_\nu+j_\nu$$

$N_\pm$: positronic/electronic spatial # density,
$E_{\|}$: mangnetic-field-aligned electric field,
$S_{\rm IC}$: ICS re-distribution function, $d\omega$: solid angle element,
I_ν: specific intensity, l : path length along the ray
α_ν: absorption coefficient, j_ν: emission coefficient

§4 Modern Outer-gap Model

Specify the three parameters: (period P is known)

- magnetic inclination (e.g., $\alpha_{\rm inc}$=45º, 75º),
- magnetic dipole moment of NS (e.g., μ=4×10^{30}G cm^3)
- neutron-star surface temperature (e.g., $kT_{\rm NS}$=50 eV)

Solve Poisson eq. + Boltzmann eqs + radiative transf. eq.

I first solved (in 6-D phase space)

- 3-D gap geometry,
- acceleration electric field distribution, $E_{\parallel}$,
- particle density and energy spectrum,
- photon specific intensity (→predicts γ-ray properties),

by specifying these three parameters, assuming ***B***-field structure by vacuum rotating dipole solution (Cheng + '00).

§5 Gamma-ray and X-ray Luminosities of MSPs

Wang & KH (2011), ApJ 736, 127

Let us first examine **millisecond pulsars**.

Before presenting numerical results, we first analytically derive the death line of MSPs on (P,$\dot{P}$) plane..

For MSPs, pair-production threshold constrains the death line. Typical Lorentz factor of in-falling e^-'s at PC:

$$\gamma \approx 2.5\times10^7\, P^{1/3}\left[\ln\left(\frac{r_{\rm null}}{r_*}\right)\right]^{-1/3}$$

Equating $\sigma T_{\rm max}{}^4$ with the energy flux deposited by the bombardment, we obtain the maximum temperature of the heated PC surface:

$$kT_{\rm max} \approx 426\ {\rm eV}\ \gamma^{1/4} P^{-1/4} \mu_{30}^{1/4}$$

§5 Gamma-ray and X-ray Luminosities of MSPs

Wang & KH (2011), ApJ 736, 127

Thus, thermal photons will have energies around keV,

$$h\nu_X \approx 3kT_{\max} \approx 0.0023\, \mathrm{m_e}c^2 P^{-1/6}\mu_{30}^{1/4} \quad (\sim \mathrm{keV})$$

While the curvature γ-rays have energies around GeV,

$$h\nu_\gamma \approx 160\, \mathrm{m_e}c^2 P^{-7/4}\mu_{30}^{3/4} \quad (\sim \text{a few GeV})$$

Therefore, the pair-production threshold,
$h\nu_X \times h\nu_\gamma > (\mathrm{m_e}c^2)^2$ gives the death line,

$$\lg \dot{P} > -14.1 + 2.83 \lg P$$

so that the pair production may be self-sustained.

§5 Gamma-ray and X-ray Luminosities of MSPs

Death lines on (P,$\dot{P}$) plane

Wang & KH (2011), ApJ 736, 127

Close-up of MSP region

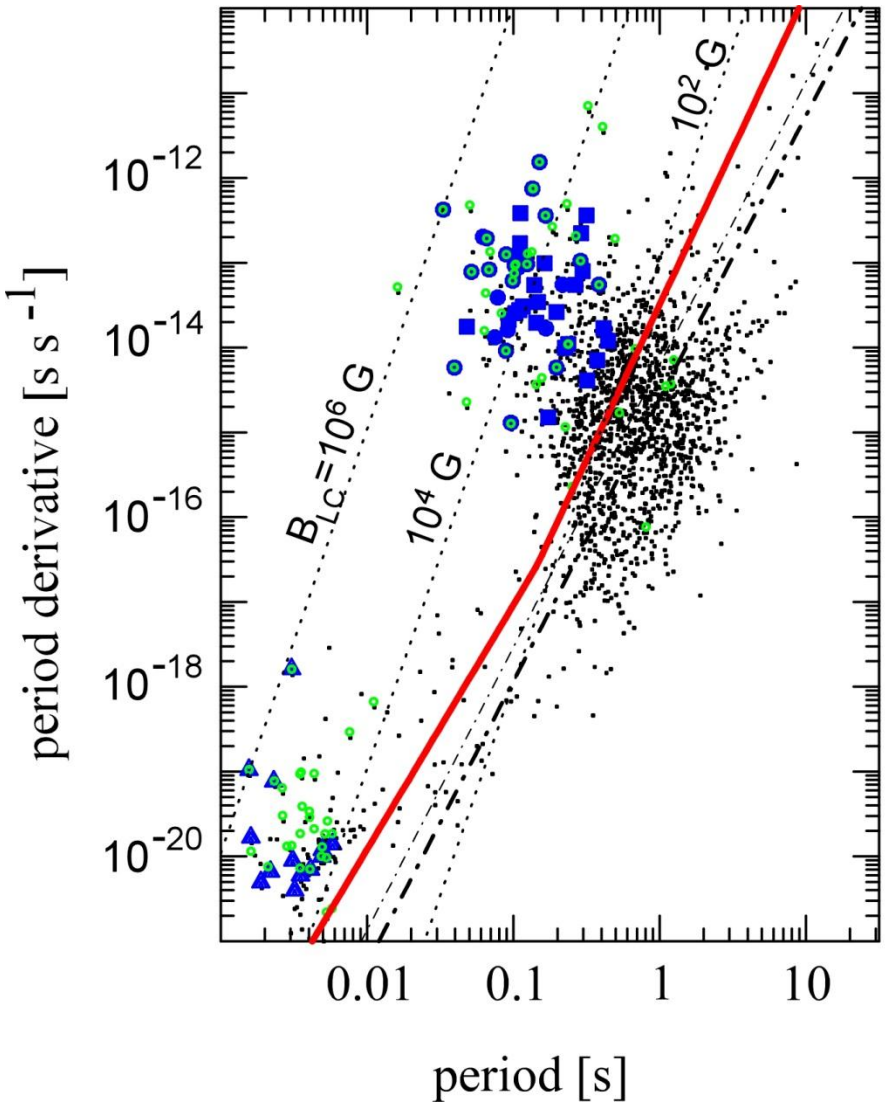

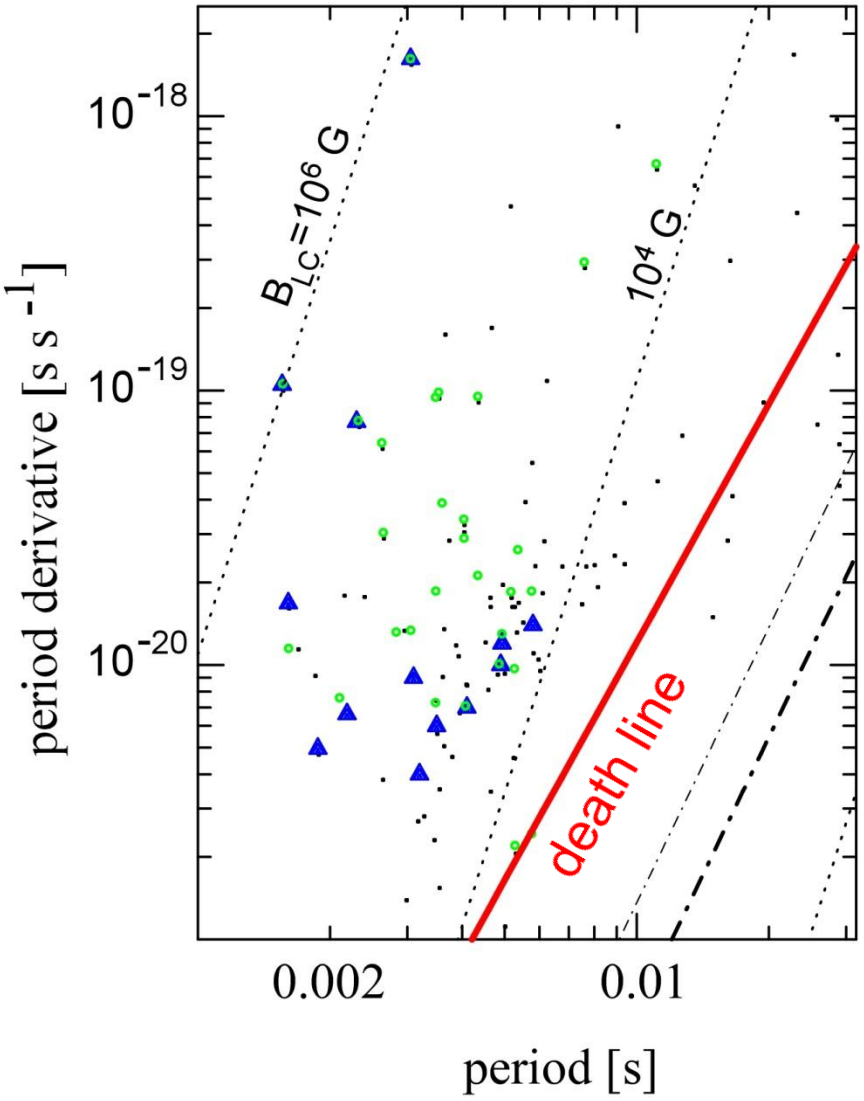

§5 Gamma-ray and X-ray Luminosities of MSPs

Next, let us numerically derive the X-ray and γ-ray luminosities on the (P,$\dot{P}$) plane and confirm the analytical death line.

Apply the numerical scheme to typical MSP parameter sets.

Advantage: For MSPs, only 3 parameters (P,dP/dt,α), or (P,μ,α) determines OG geometry, $E_{\|}$ distribution, $e^{\pm}$ distribution functions, and specific intensity uniquely, because the whole NS surface X-ray emission is not important.

§5 Gamma-ray and X-ray Luminosities of MSPs

Wang & KH (2011), ApJ 736, 127

An example of the solved distribution of created current density and the temperature on the PC surface:

Ex) P=10 ms, $\dot{P}$=10^{-19} s/s, α=60°

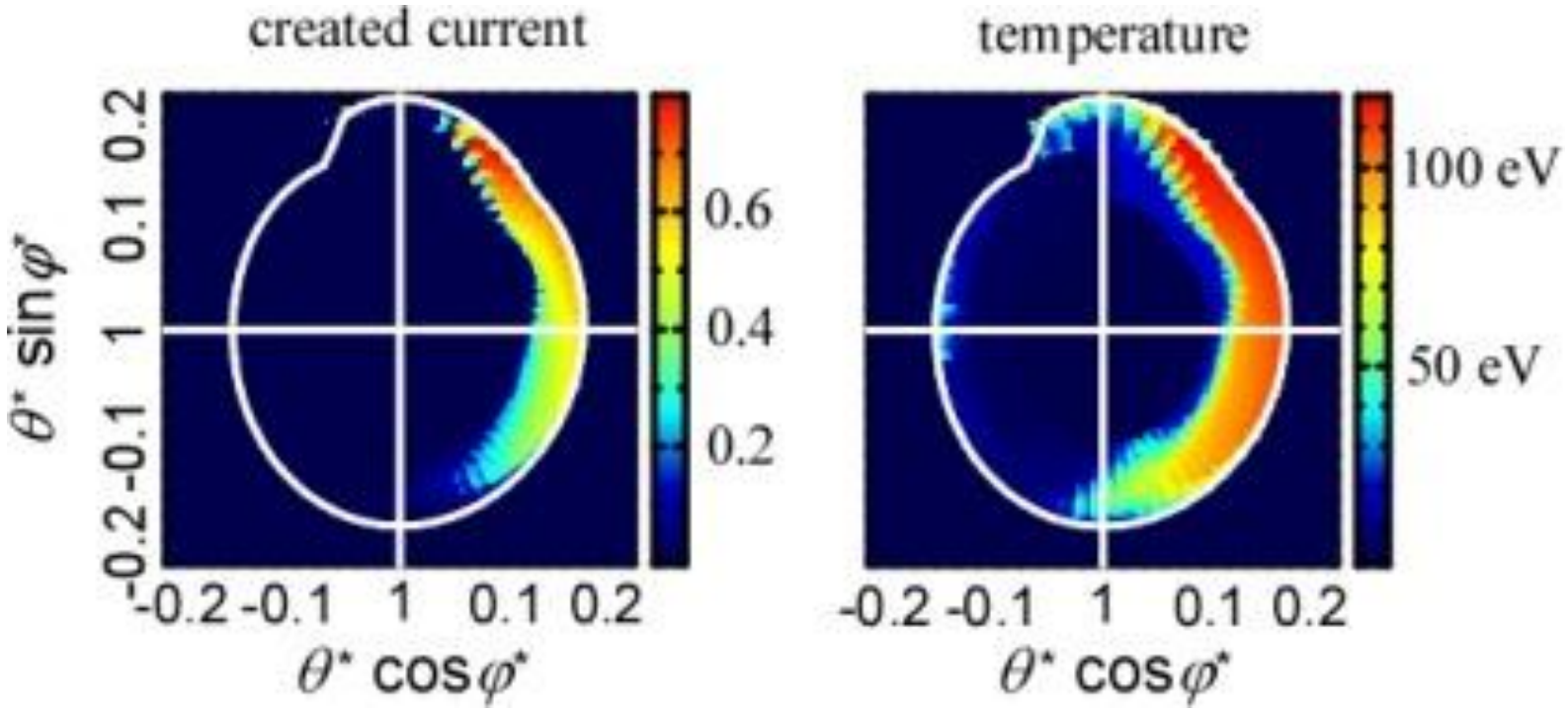

(Heat conduction in trans-**B** direction is not considered.)

§5 Gamma-ray and X-ray Luminosities of MSPs

Solve OG for 20 MSP parameter sets.

Distribution of γ-ray luminosity:

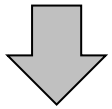

γ-ray only MSPs?

(magnetospheric components only; PWS excluded)

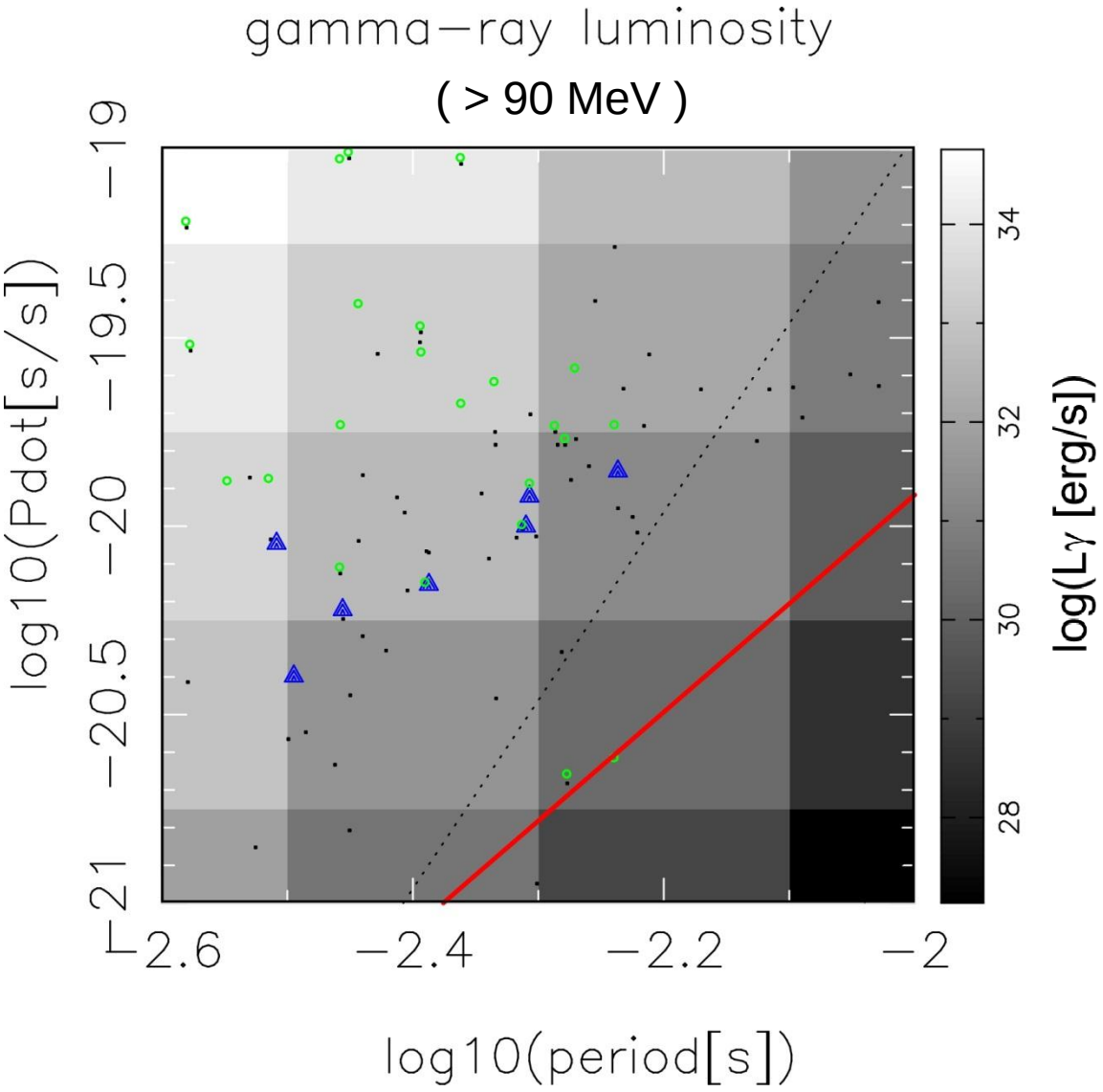

§5 Gamma-ray and X-ray Luminosities of MSPs

Solve OG for 20 MSP parameter sets.

Distribution of X-ray luminosity of heated PC:

(magnetospheric components only; PWS excluded)

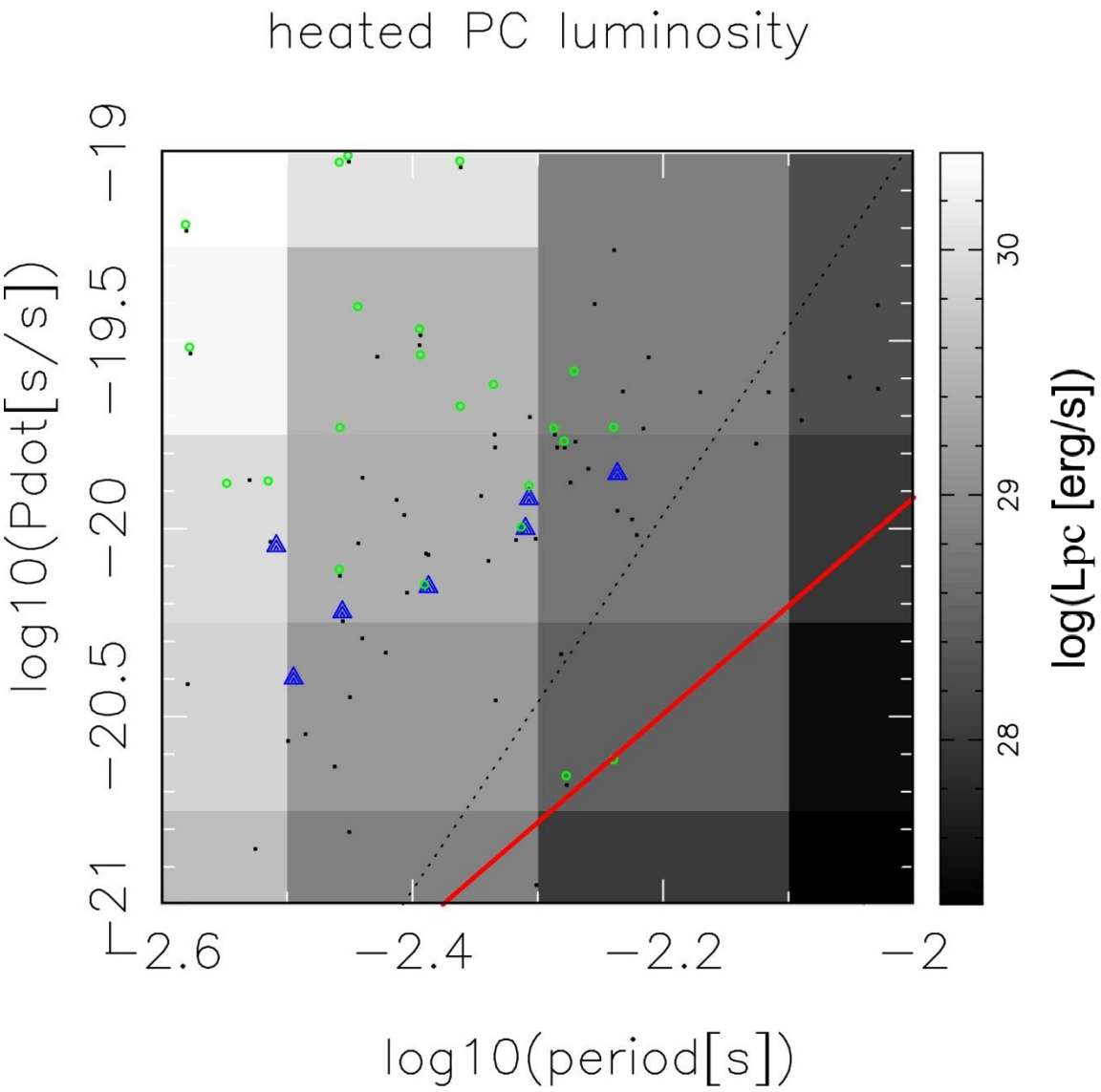

§6 Evolution of Spectral Hardness

Next, let us show that the trailing peak has a harder spectrum than the leading peak in GeV energies.

In the OG, γ-rays are emitted by curvature process.

Characteristic energy of curvature emission:

$$E_c = \frac{3hc}{4\pi}\frac{\gamma^3}{\rho_c}$$

Electro-static force balance

$$eE_{\parallel} = \frac{2e^2\gamma^4}{3\rho_c{}^2}$$

γ : Lorentz factor

ρ_c : curvature radius

Eliminate γ →

$$E_c = \left(\frac{3}{2}\right)^{7/4}\frac{hc}{2\pi}\rho_c{}^{1/2}\left(\frac{E_{\parallel}}{e}\right)^{3/4}$$

§6 Evolution of Spectral Hardness

KH (2011), ApJ 733, L49

Characteristic energy of curvature emission:

$$E_c = \left(\frac{3}{2}\right)^{7/4} \frac{hc}{2\pi} \rho_c^{1/2} \left(\frac{E_{\parallel}}{e}\right)^{3/4}$$

Above E_c , the flux density sharply declines as

$$F_\nu \propto \left(\frac{E}{E_c}\right)^{1/2} \exp\left(-\frac{E}{E_c}\right)$$

Thus, the cut-off energy, E_c, increases with increasing ρ_c.

§6 Evolution of Spectral Hardness

KH (2011), ApJ 733, L49

Because of rotation, the curvature radius, ρ_c, of particle paths becomes greater in the trailing side (TS).

↓

Greater E_c in TS

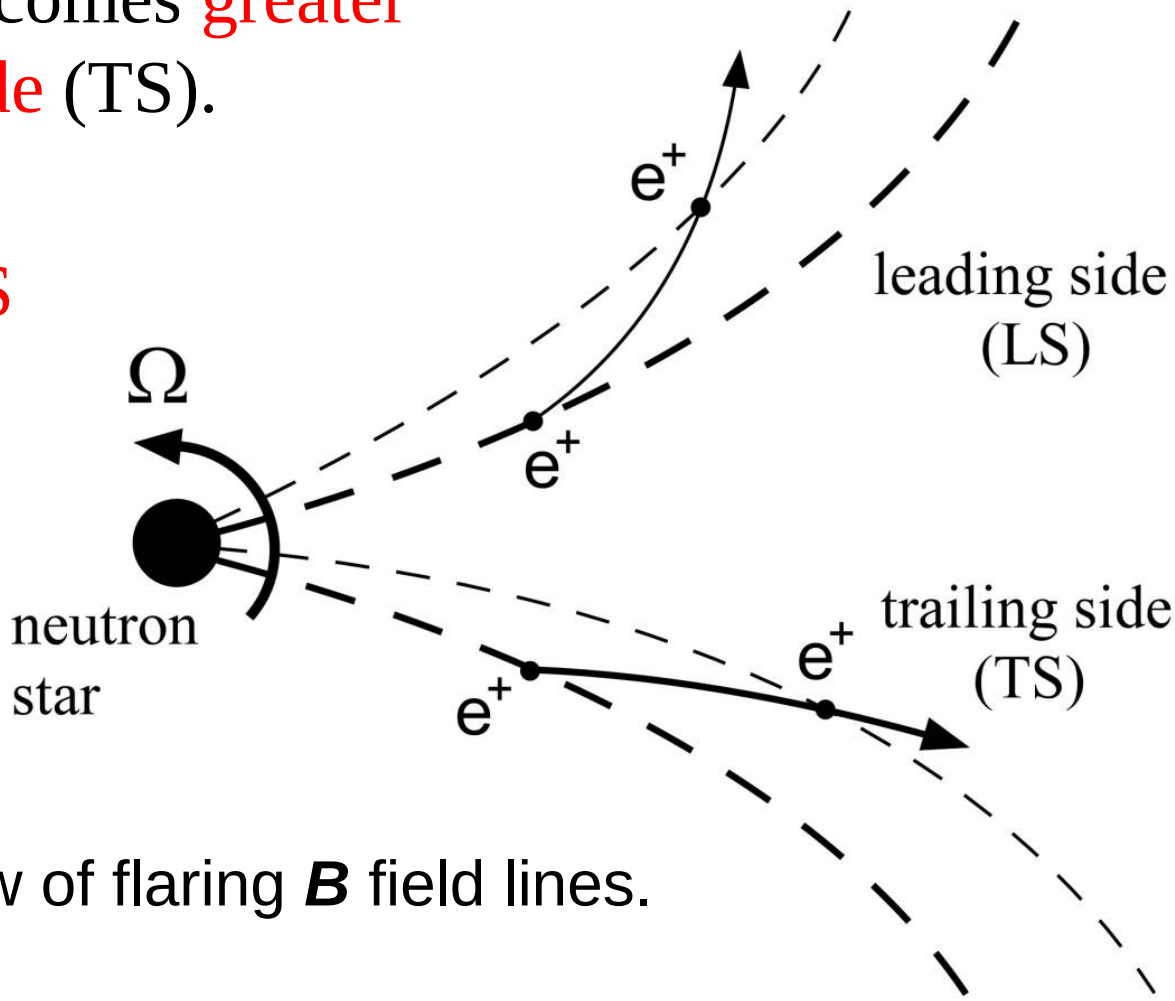

Top view of flaring ***B*** field lines.

§6 Evolution of Spectral Hardness

KH (2011), ApJ 733, L49

Quantitative discussion: ρ_c of actual particle paths.

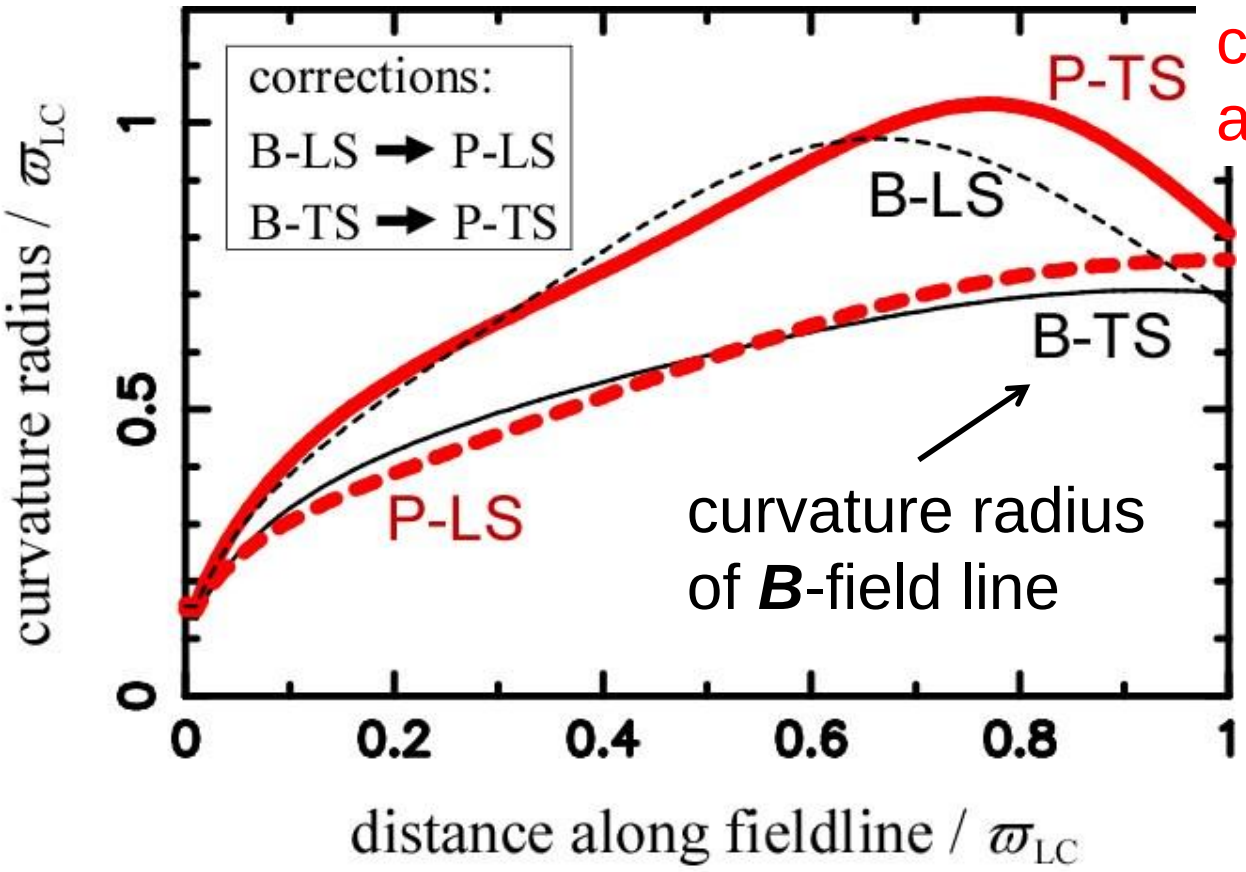

curvature radius of actual particle path

TS: φ^*=-60°

LS: φ^*= 60°

φ^*: magnetic azimuth

§6 Evolution of Spectral Hardness

KH (2011), ApJ 733, L49

To compute E_c, we also need $E_{\|}$, in addition to ρ_c.

$$E_c = \left(\frac{3}{2}\right)^{7/4} \frac{hc}{2\pi} \rho_c^{1/2} \left(\frac{E_{\|}}{e}\right)^{3/4}$$

Solve $E_{\|}$ from the set of Maxwell & Boltzmann eqs.

↓

Photon specific intensity

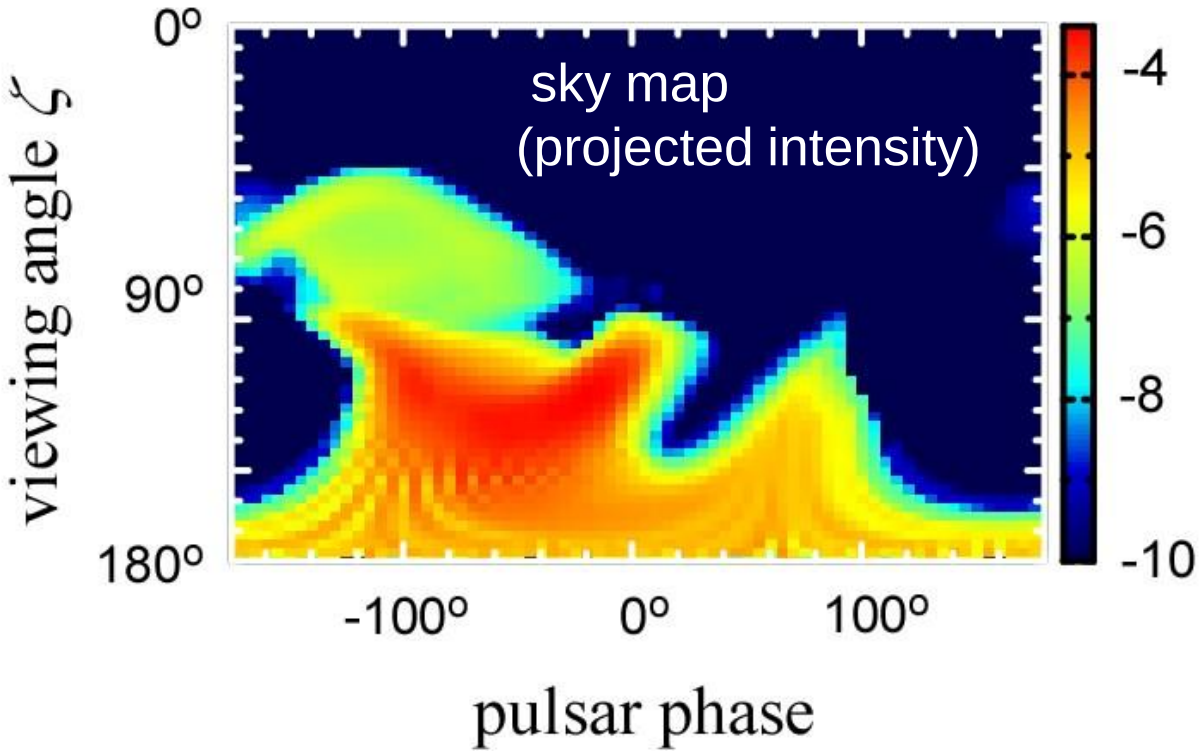

§6 Evolution of Spectral Hardness

Ex.) typical young pulsar

KH (2011), ApJ 733, L49

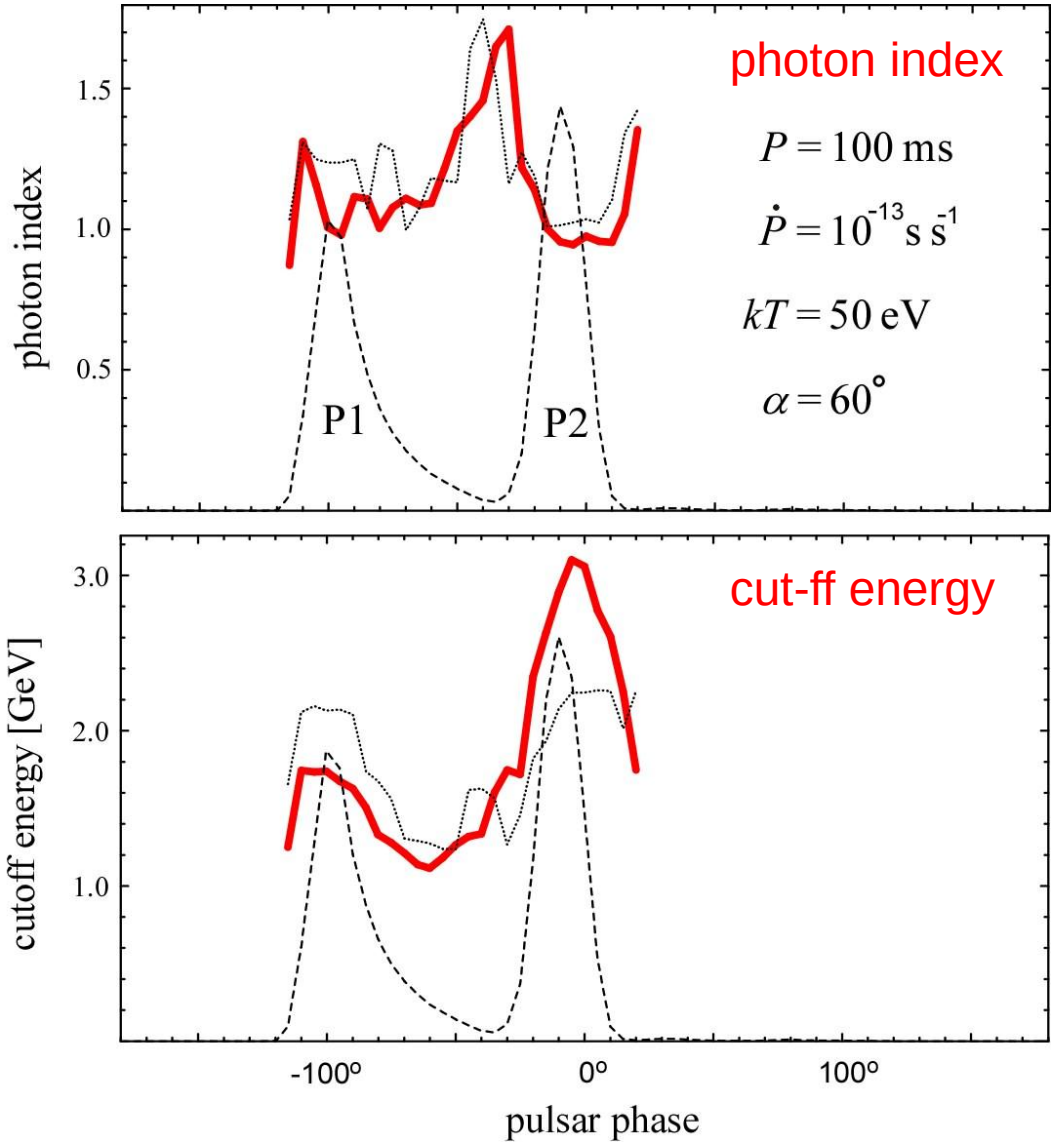

E_c

Energy-dependent sky map

↓

Phase-resolved spectra of any pulsars

P2 has greater E_c.
(applicable not only to MSPs, but rotation-powered PSRs in general)

§6 Evolution of Spectral Hardness

The hard P2 spectrum is consistent with observations.

So far, detailed phase-resolved spectra have been obtained from 7 pulsars with LAT.

Fitting spectra by power-law + exp.-cutoff,

$$\frac{dN}{dE} = KE^{-\Gamma} \exp\left(-\frac{E}{E_c}\right),$$

they find E_c becomes greater in P2 than in P1.

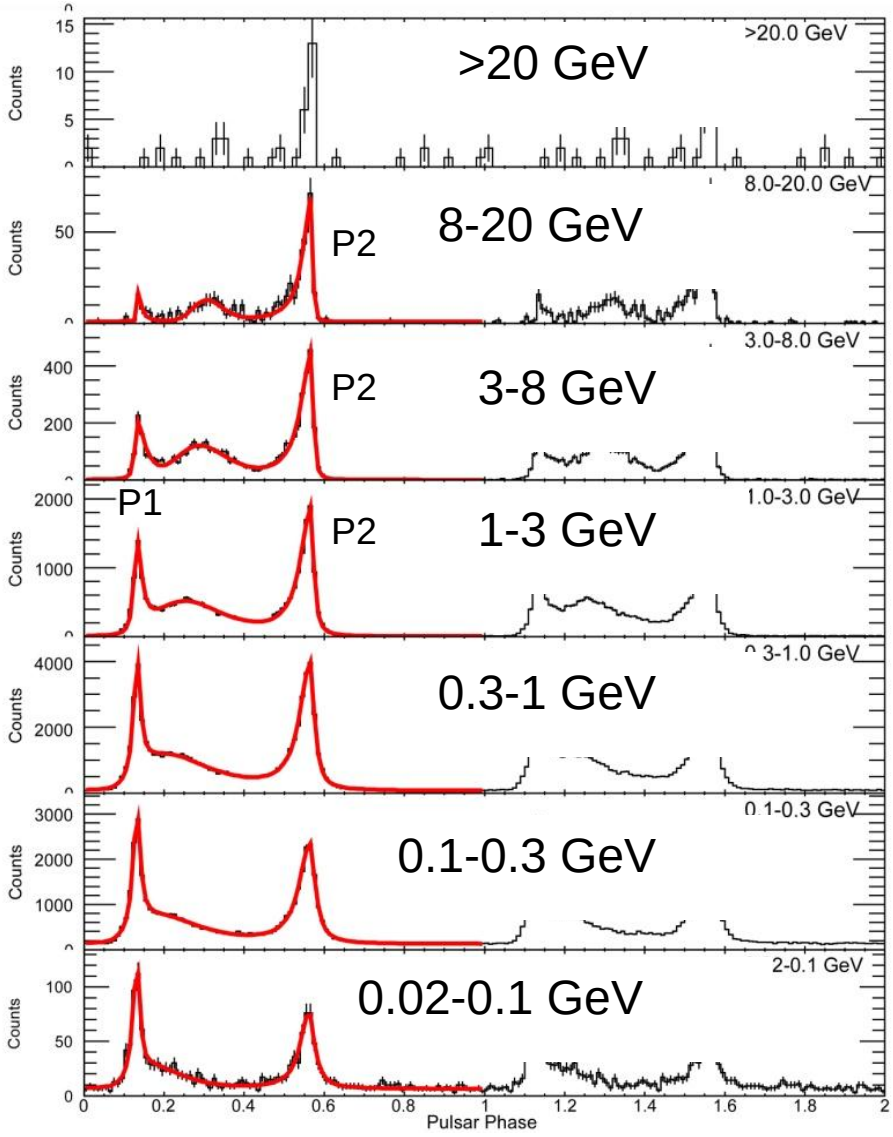

§6 Evolution of Spectral Hardness

Crab pulsar ($\tau \sim 1$ kyr)

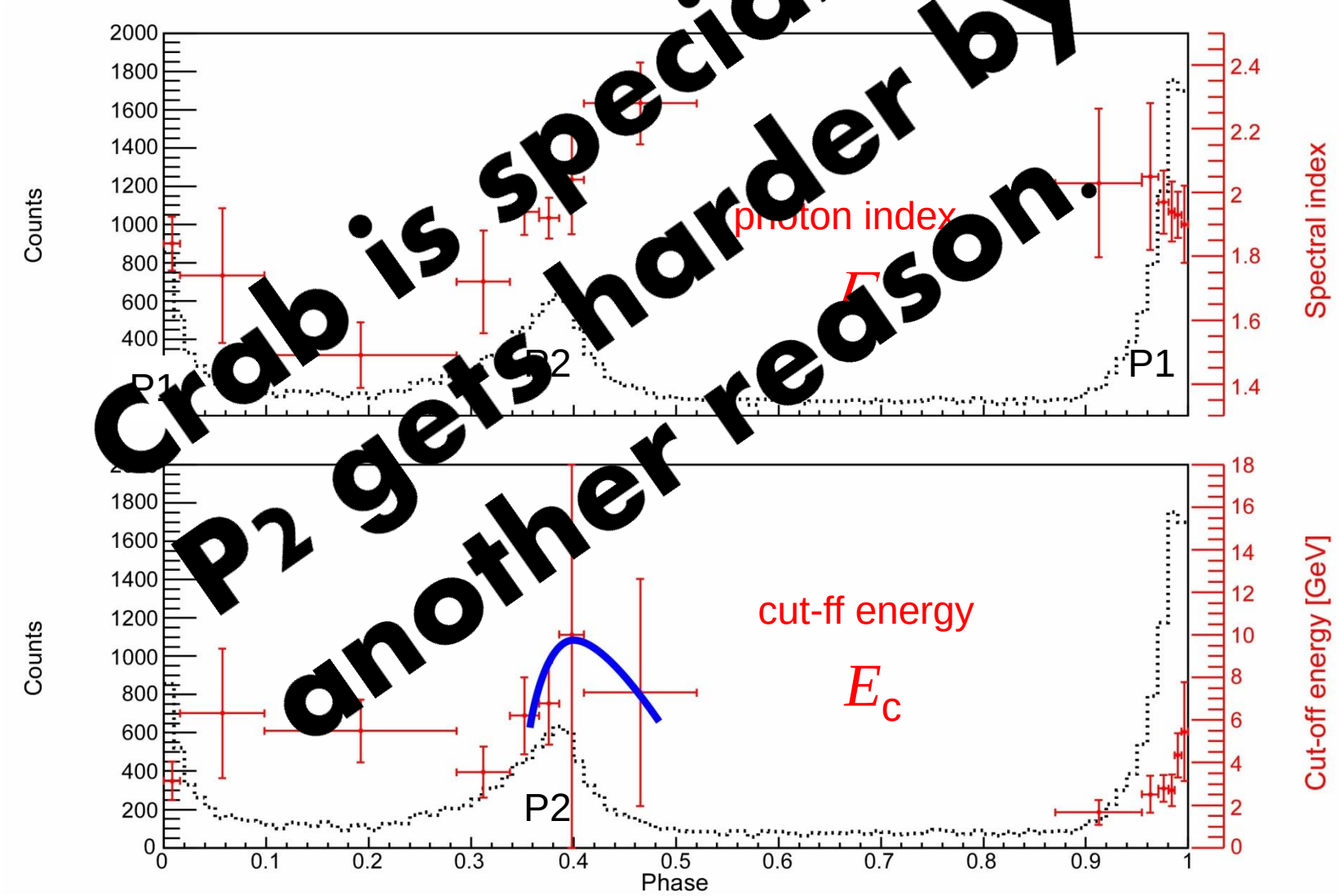

§6 Evolution of Spectral Hardness

Vela pulsar
($\tau \sim 11$ kyr)

Γ

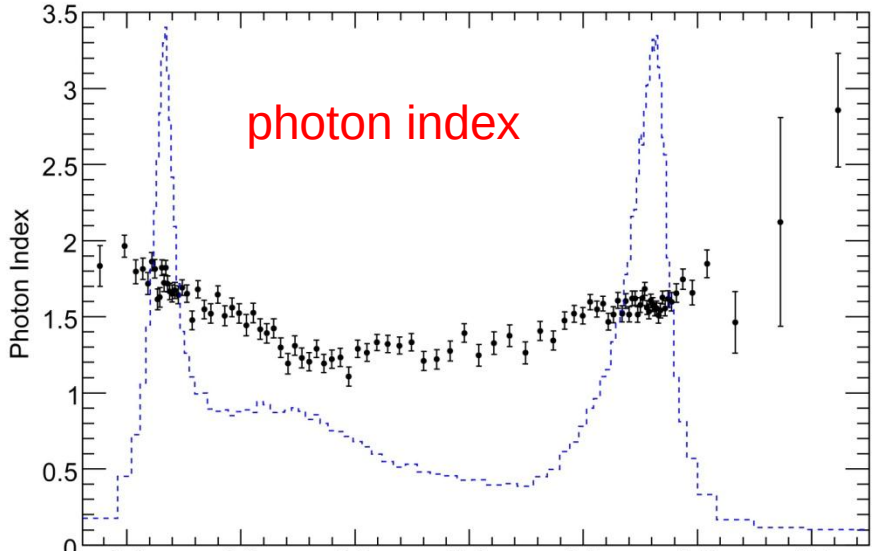

E_c

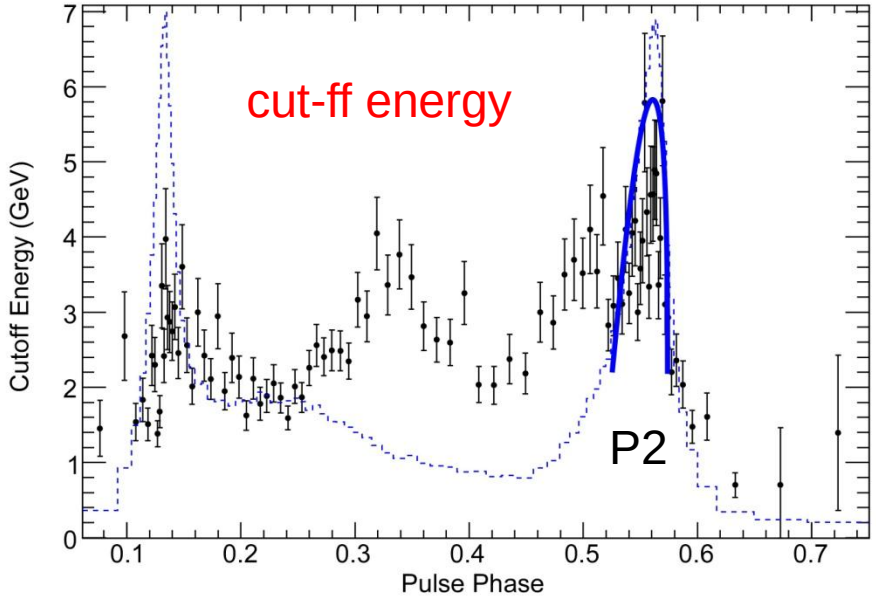

§6 Evolution of Spectral Hardness

PSR J1709-4429
(τ ~ 18 kyr)

Γ

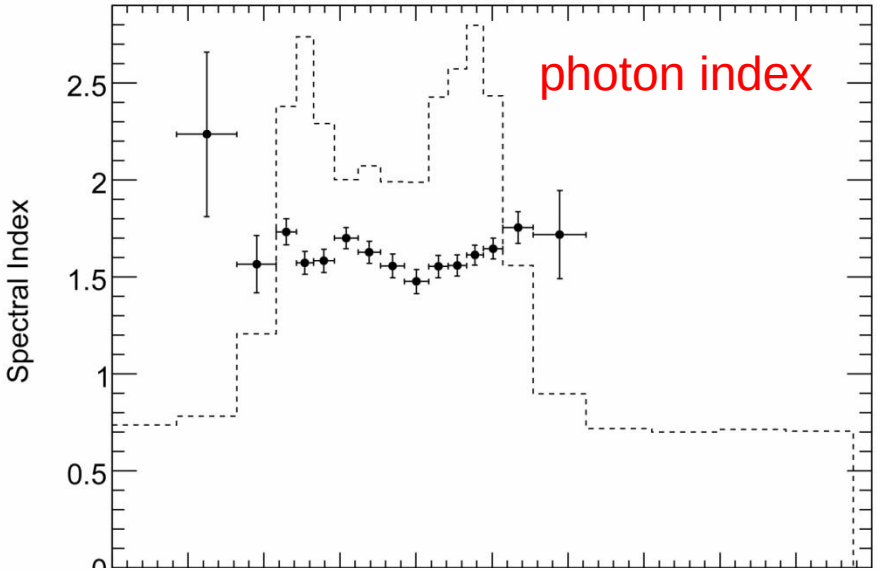

E_c

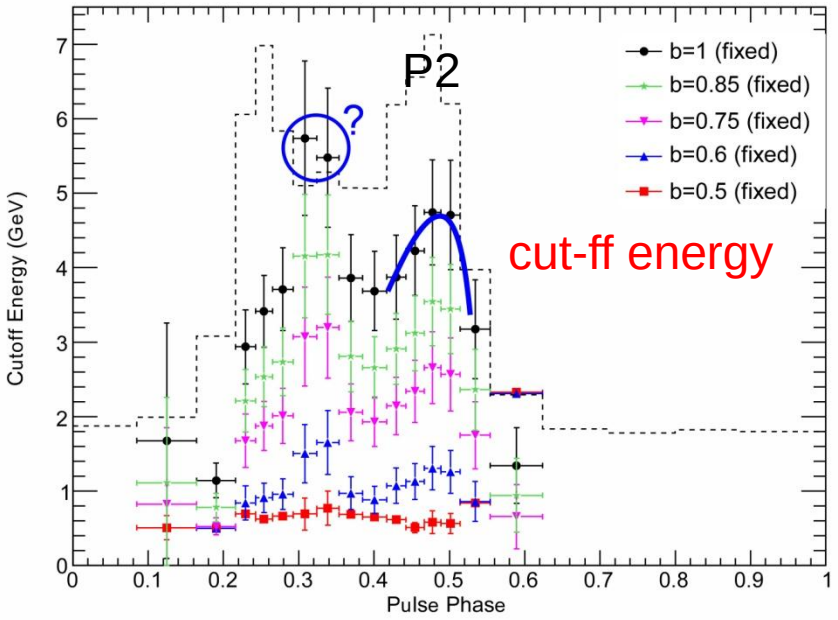

§6 Evolution of Spectral Hardness

PSR J1952+3252
($\tau \sim 110$ kyr)

Γ

E_c

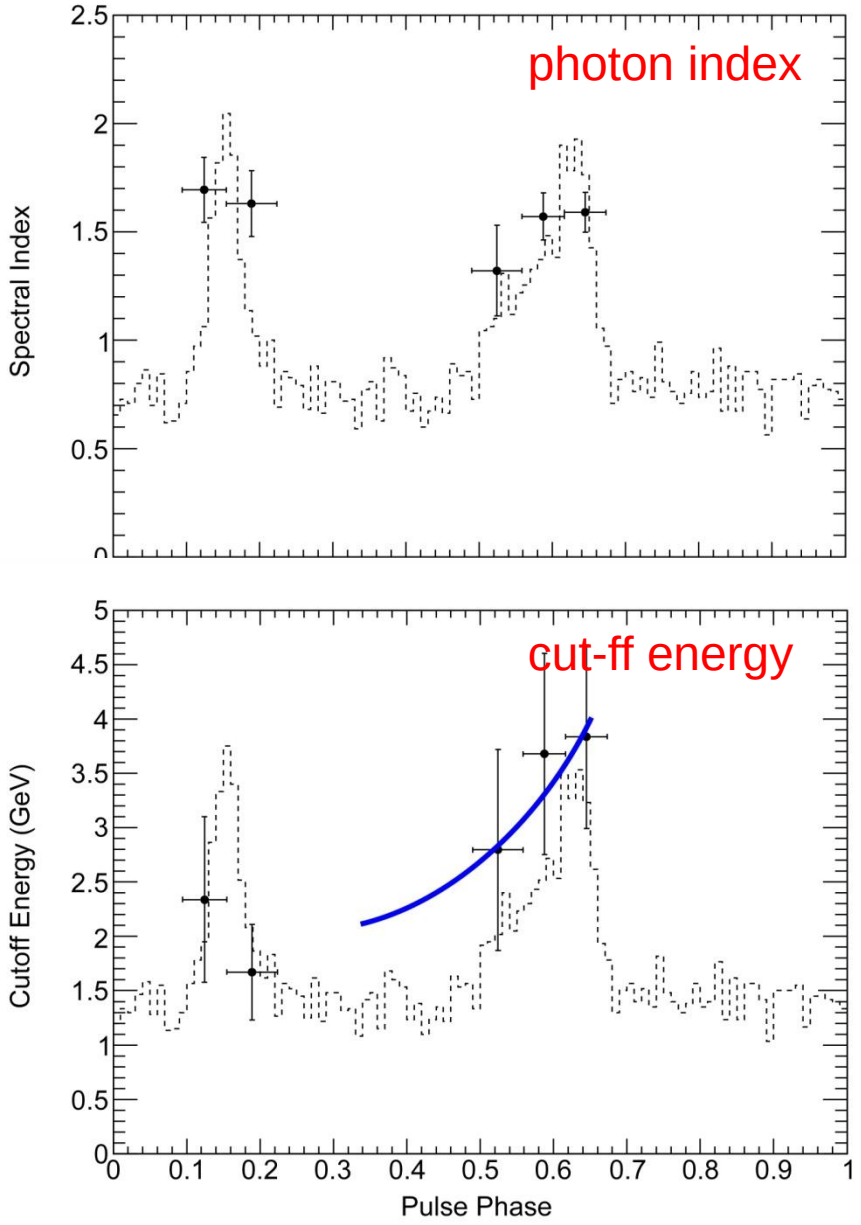

§6 Evolution of Spectral Hardness

Geminga
($\tau \sim 340$ kyr)

Γ

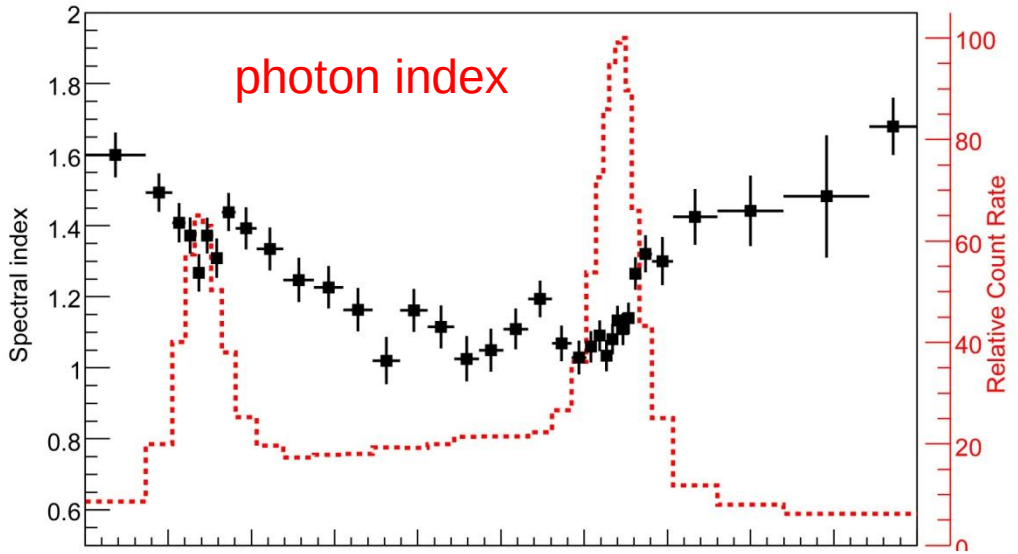

Spectral hardening
in the second,
trailing peak

E_c

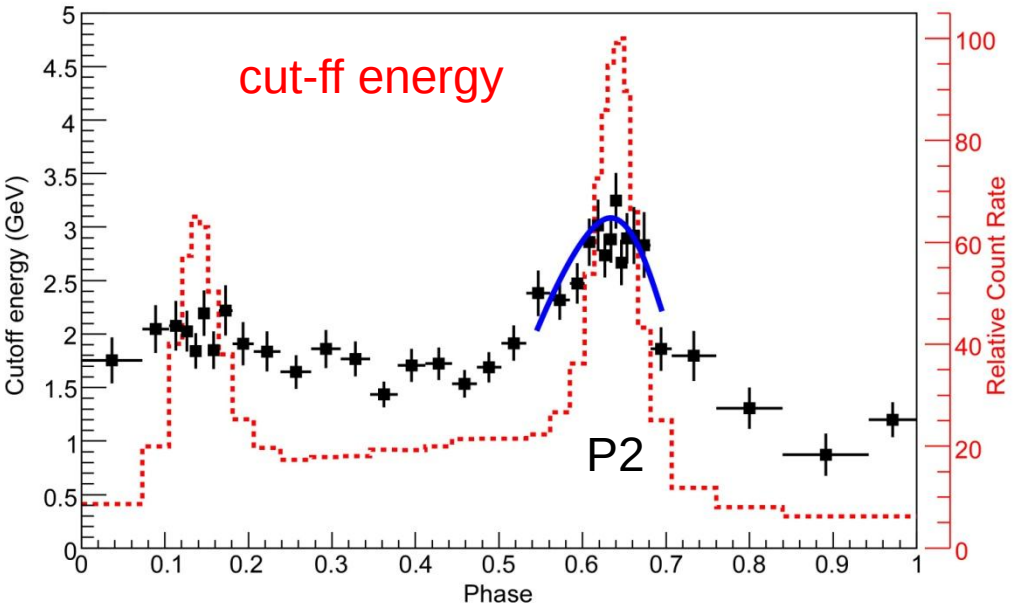

§6 Evolution of Spectral Hardness

PSR J1057-5226
(τ ~ 540 kyr)

Γ

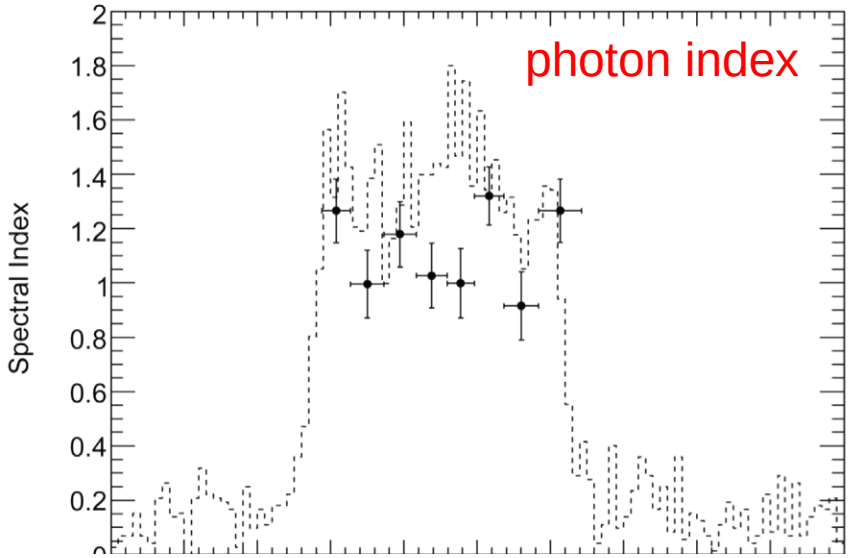

Spectral hardening occurs in the trailing side (maybe P2) of light-curve peaks.

E_c

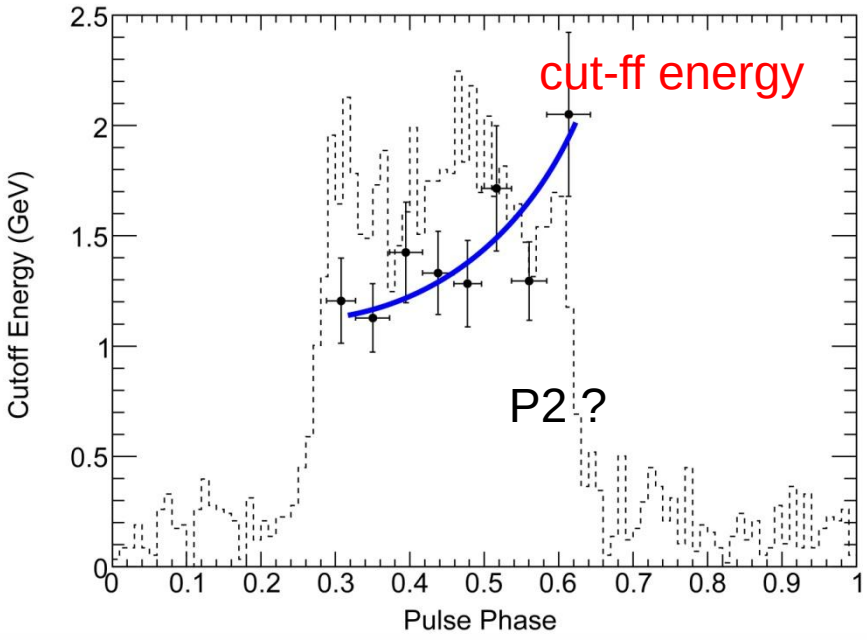

§6 Evolution of Spectral Hardness

KH (2011), ApJ 733, L49

In short, hard P2 spectra can be generally interpreted by the greater curvature radii in the trailing side of a pulsar magnetosphere.

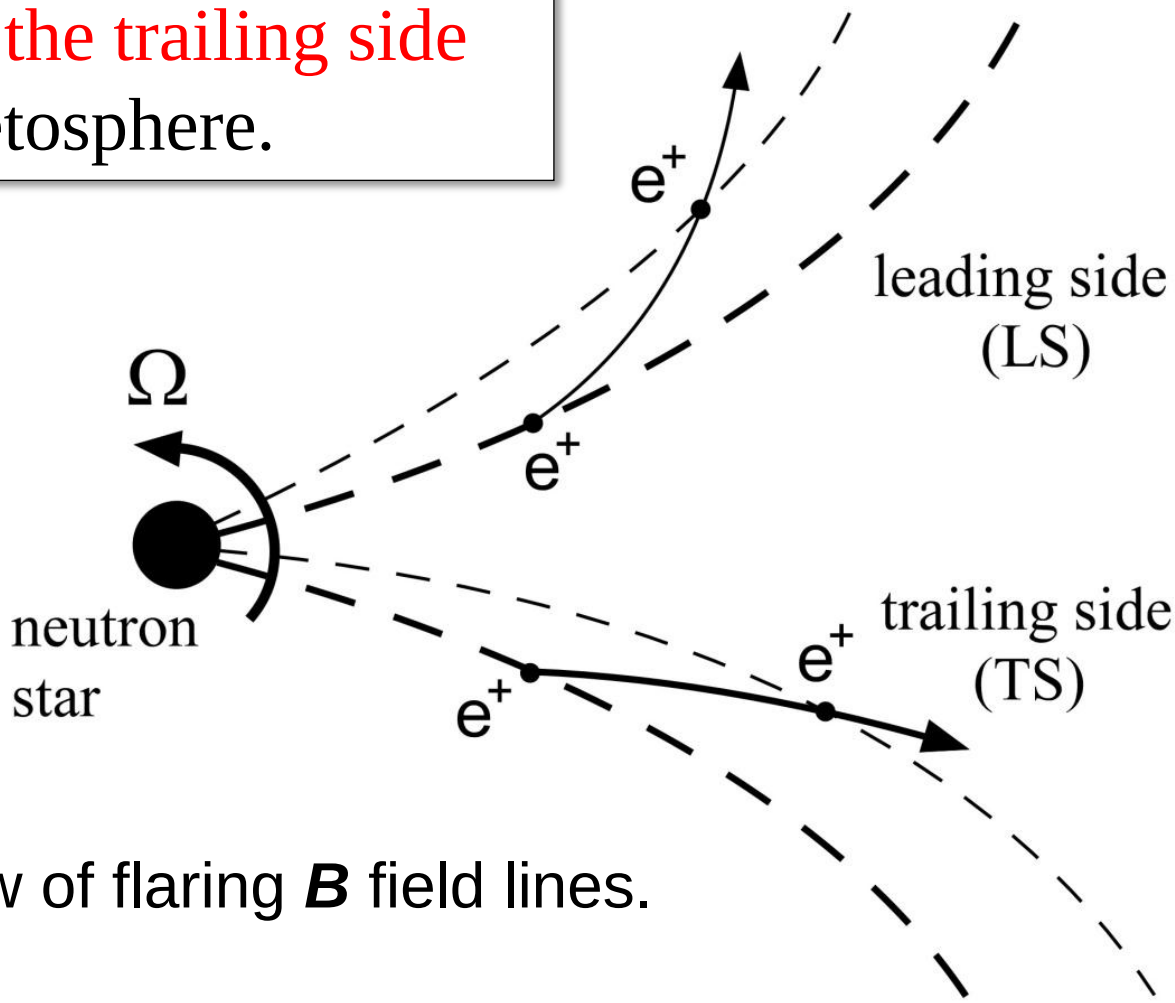

Top view of flaring ***B*** field lines.

§7 ICS spectrum of the Crab pulsar

Finally, let us numerically examine the Crab pulsar.

Maxwell & Boltzmann eqs., ⇒

- OG 3-D geometry,
- $E_{\parallel}$ distribution,
- e^+/e^- distribution functions,
- photon specific intensity

Apply this method to the Crab pulsar, assuming
$\mu = 3.8 \times 10^{30}$ G cm^3, $\alpha = 60^o$, kT= 70 eV.

§7 ICS spectrum of the Crab pulsar

3-D distribution of the particle accelerator (i.e., high-energy emission zone) solved from the Poisson eq.:

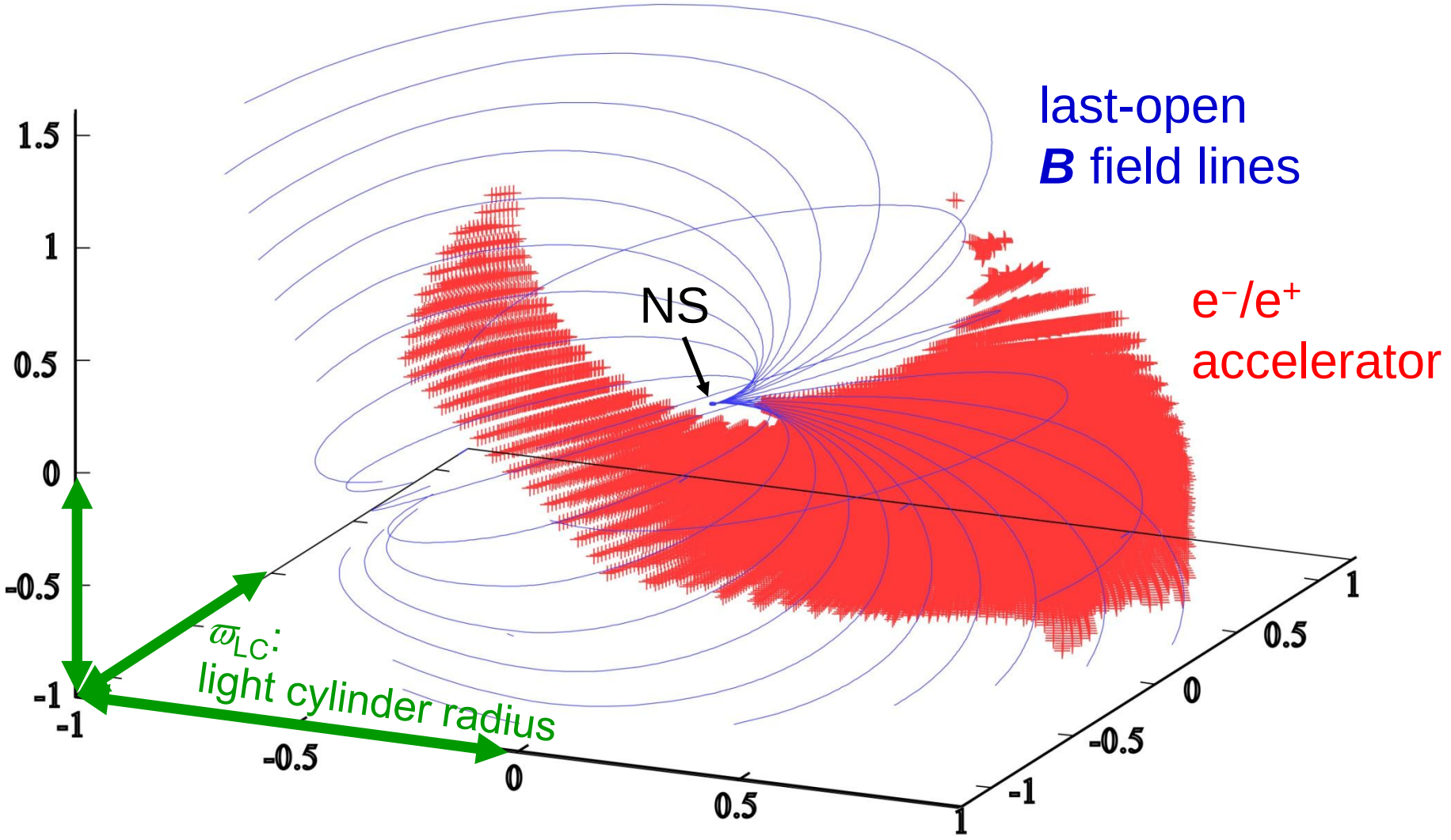

§7 ICS spectrum of the Crab pulsar

3-D geometry: Trans-field gap thickness is self-regulated by pair production.

Crab, α=60°

Fractional gap thickness projection on the last-open ***B*** line surface

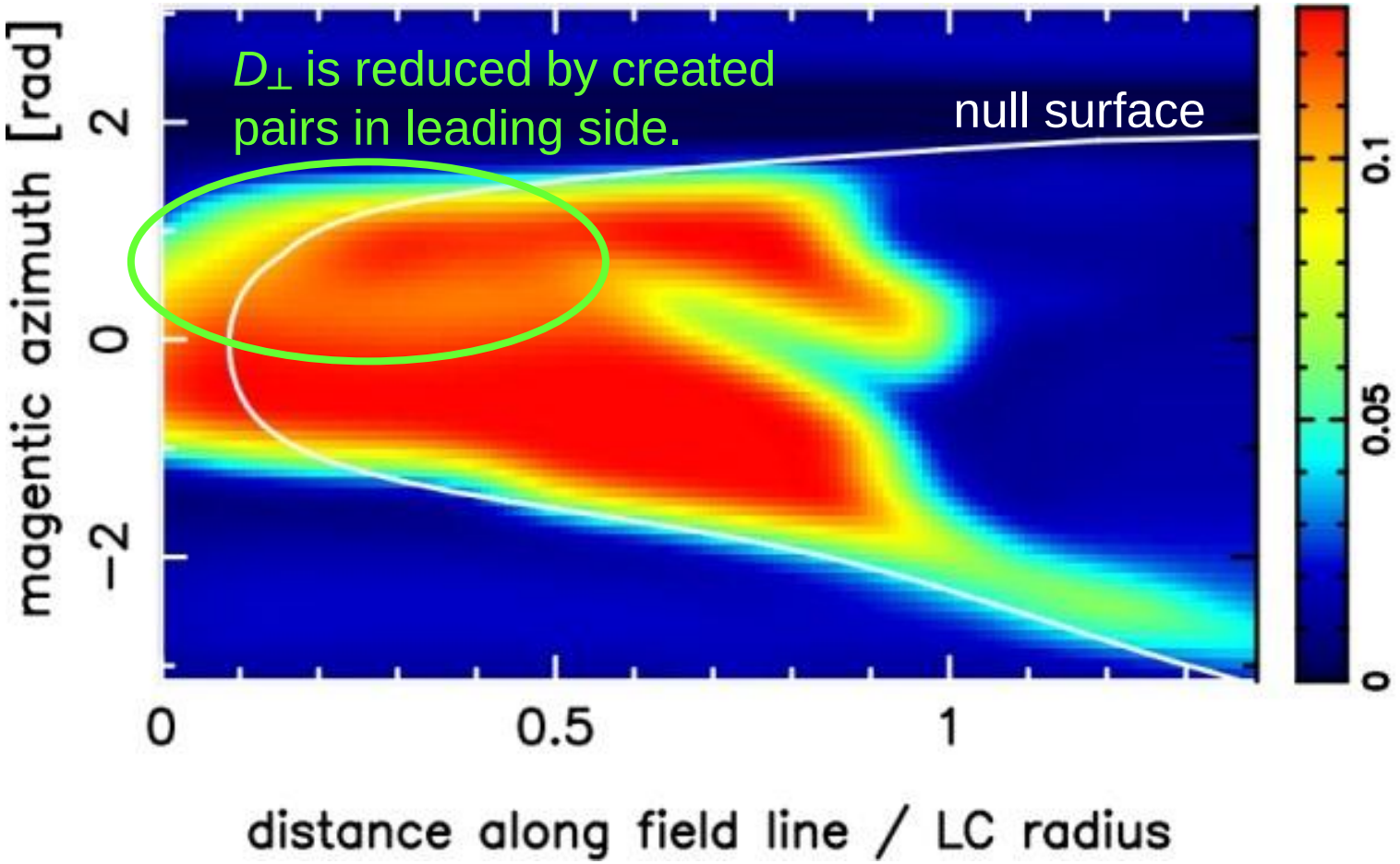

§7 ICS spectrum of the Crab pulsar

$E_{\parallel}$ is also self-regulated by pair production.

(→ Curvature photon energy changes little for various pulsars.)

Crab, α=60°

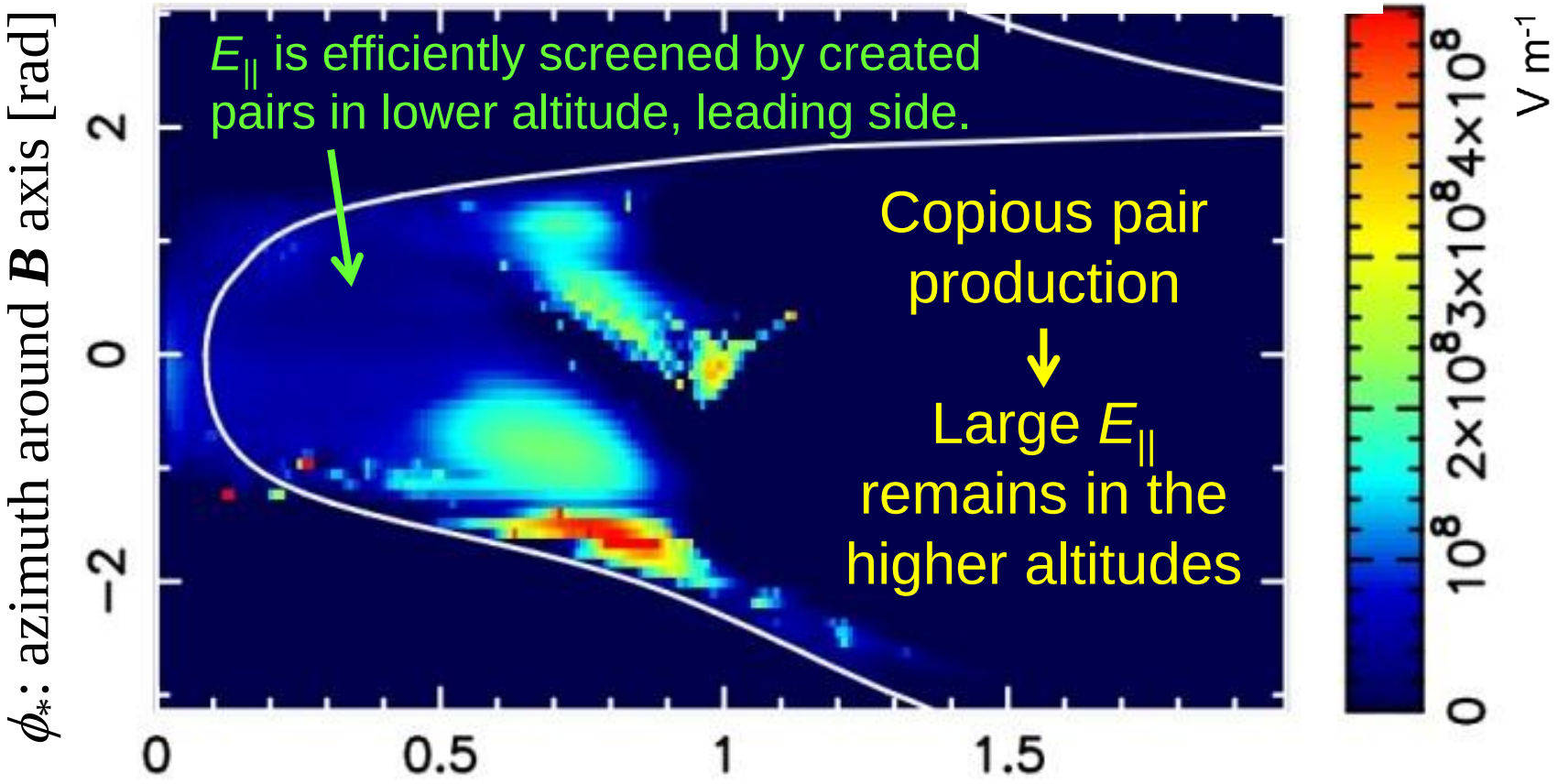

s: distance along $\boldsymbol{B}$ field lines / light-cylinder radius

§7 ICS spectrum of the Crab pulsar

$E_{\parallel}$ is also self-regulated by pair production.

(→ Curvature photon energy changes little for various pulsars.)

Crab, α=60°

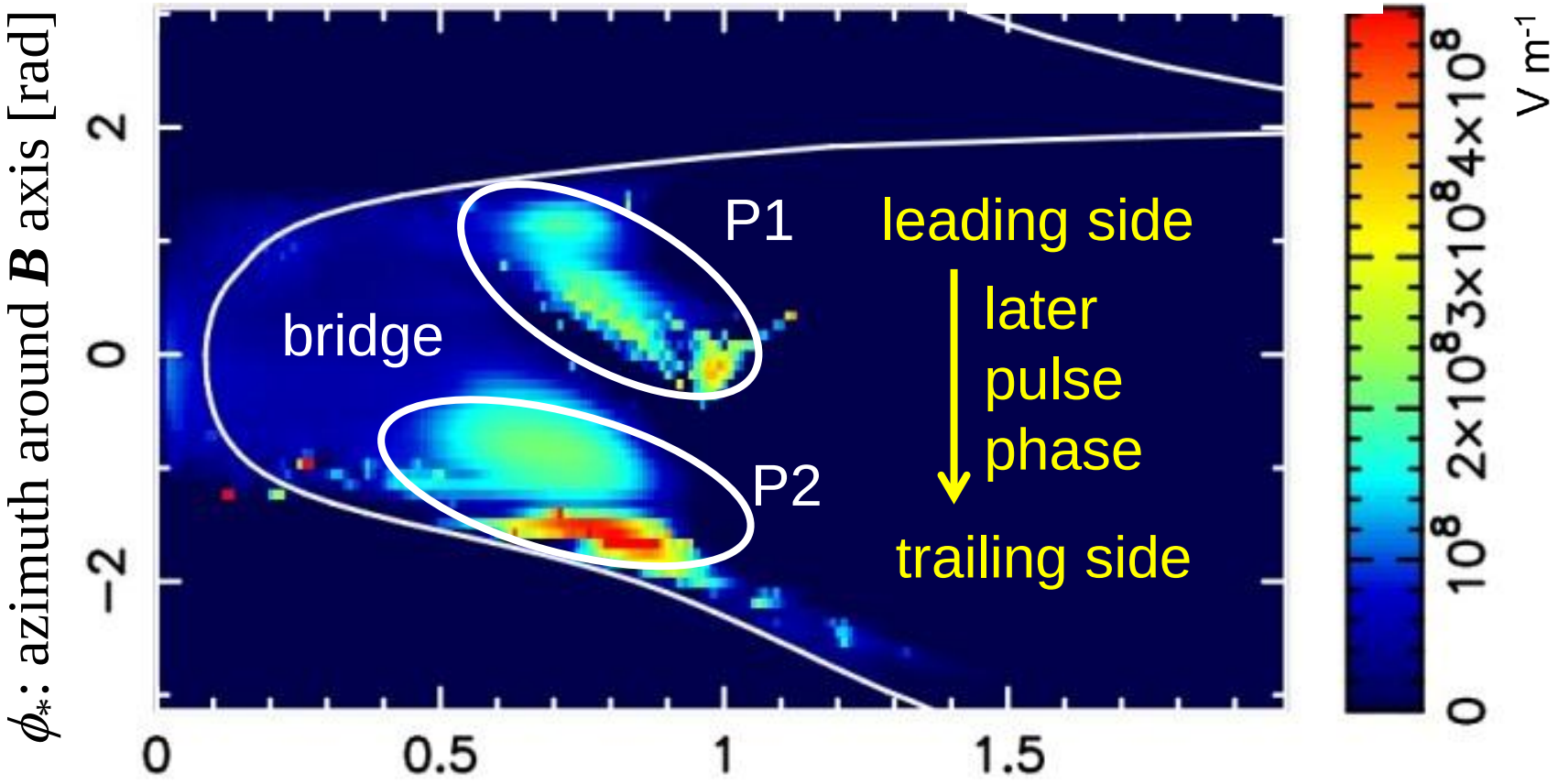

s: distance along $\boldsymbol{B}$ field lines / light-cylinder radius

§7 ICS spectrum of the Crab pulsar

Crab 60°

Using the solved $E_{||}$, we can compute emissivity at each position.

Intensity distribution shows a caustic pattern in the sky map.

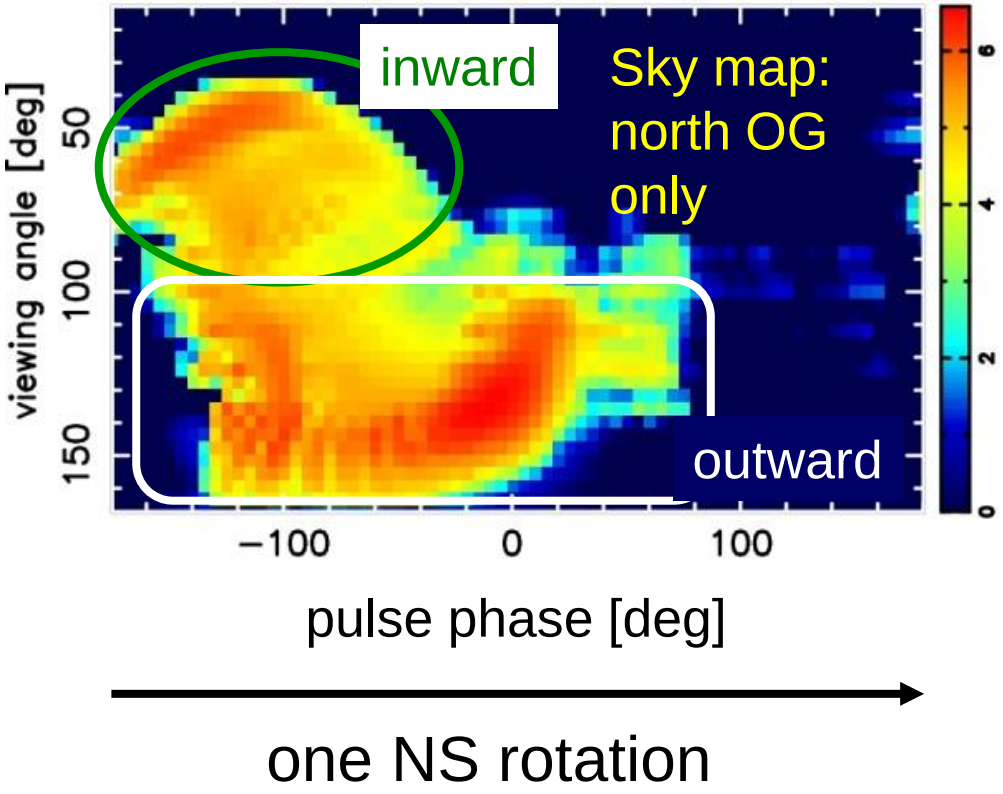

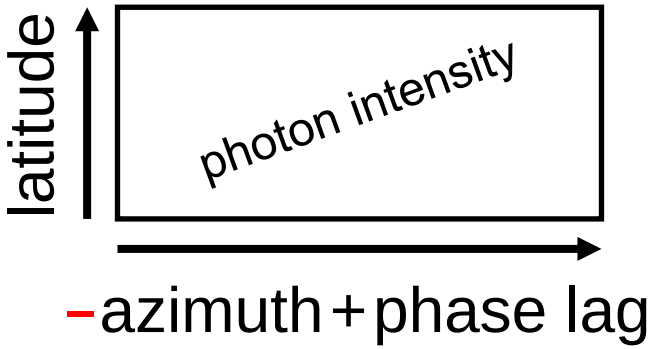

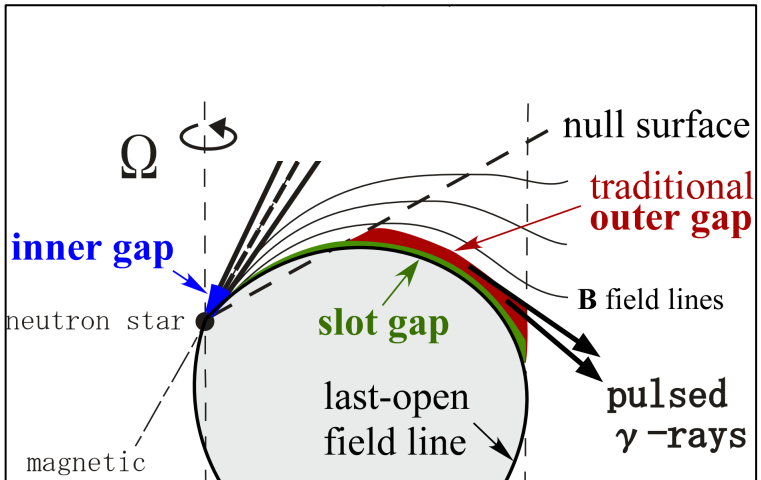

§7 ICS spectrum of the Crab pulsar

Crab 60°

To compute pulsar emissions, we must consider the photons emitted from OGs connected to the both poles.

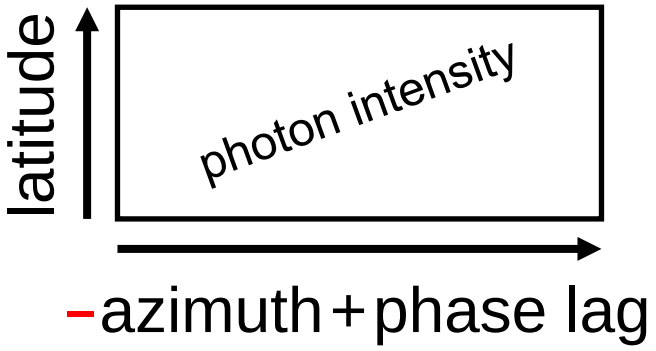

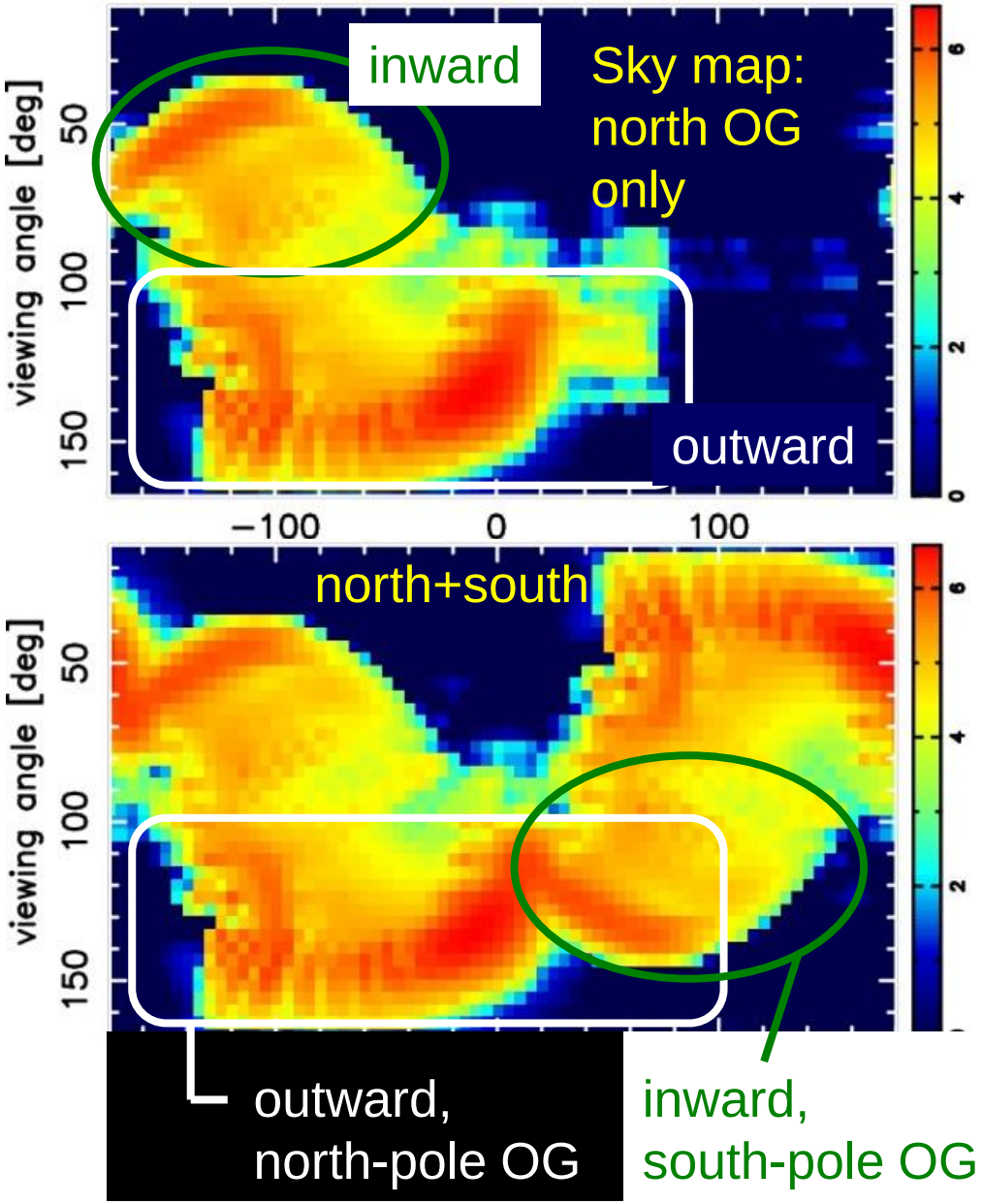

§7 ICS spectrum of the Crab pulsar

Crab 60°

If we cut the sky map at some viewing angle ζ, we obtain a pulse profile.

Using an energy-dependent sky map, we obtain pulse profiles at different energy bands.

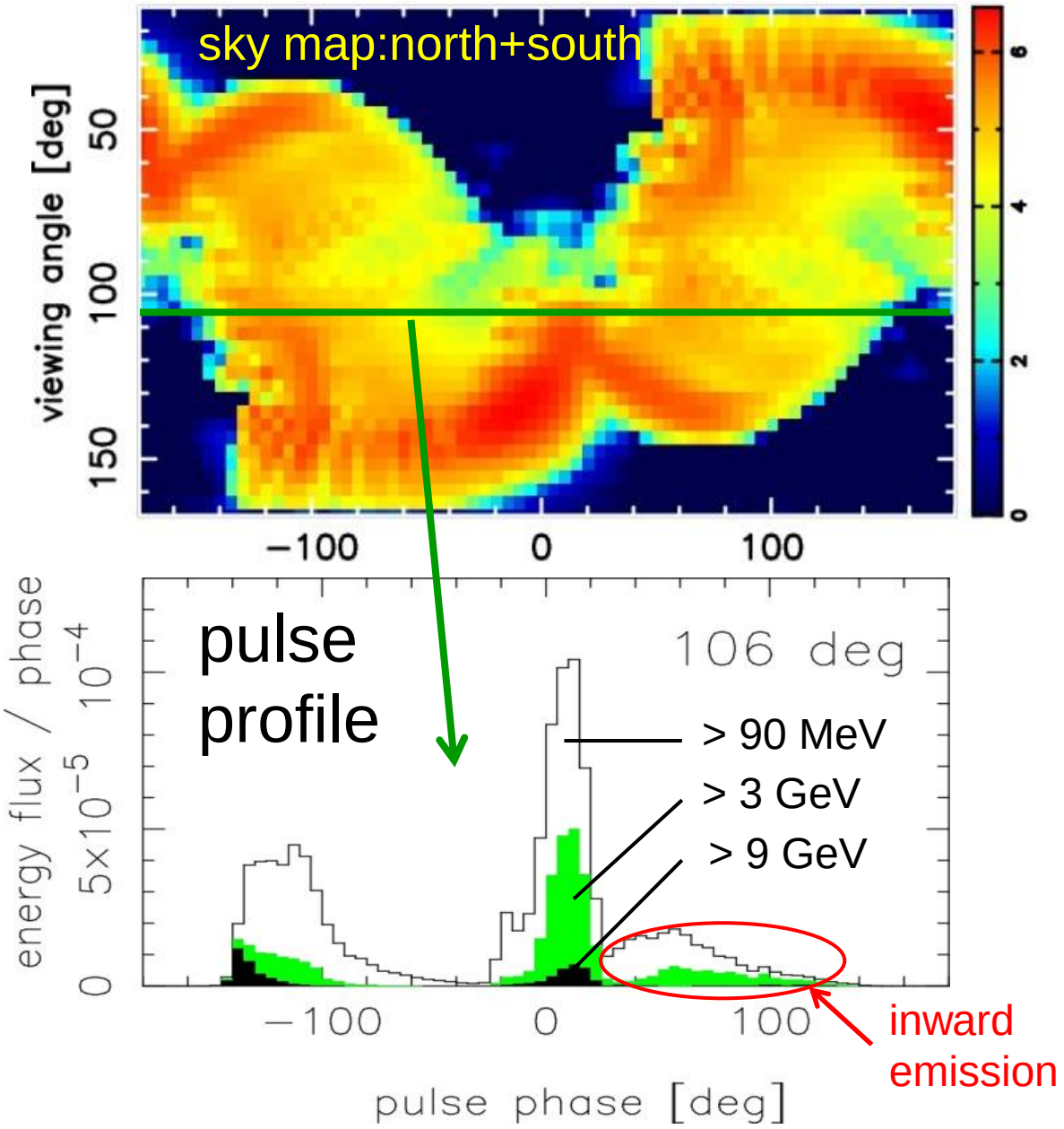

§7 ICS

If we look at the details, however, the energy-dependent pulse profile (incl. 30-400 GeV) does not reproduce the MAGIC observations.

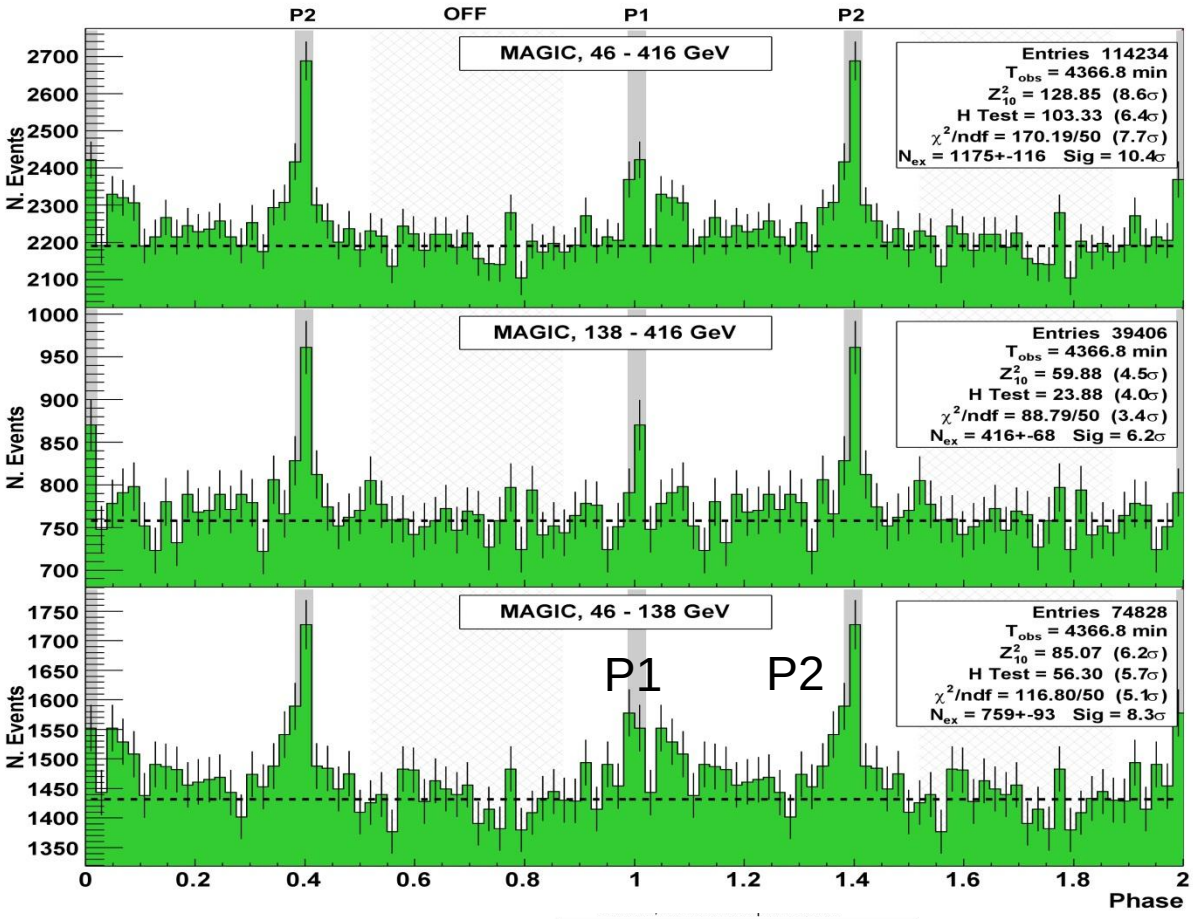

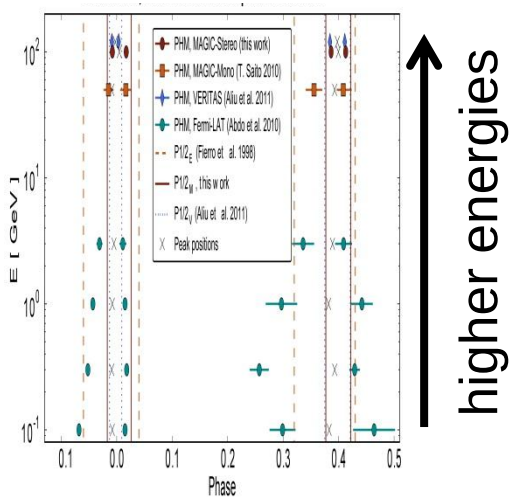

higher energies

§7 ICS spectrum of the Crab pulsar

However, my simulation shows that P1 shifts into earlier phase at higher energies !

This is because I adopt the vacuum rotating dipole ***B*** field solution, which is wrong near the light cylinder.

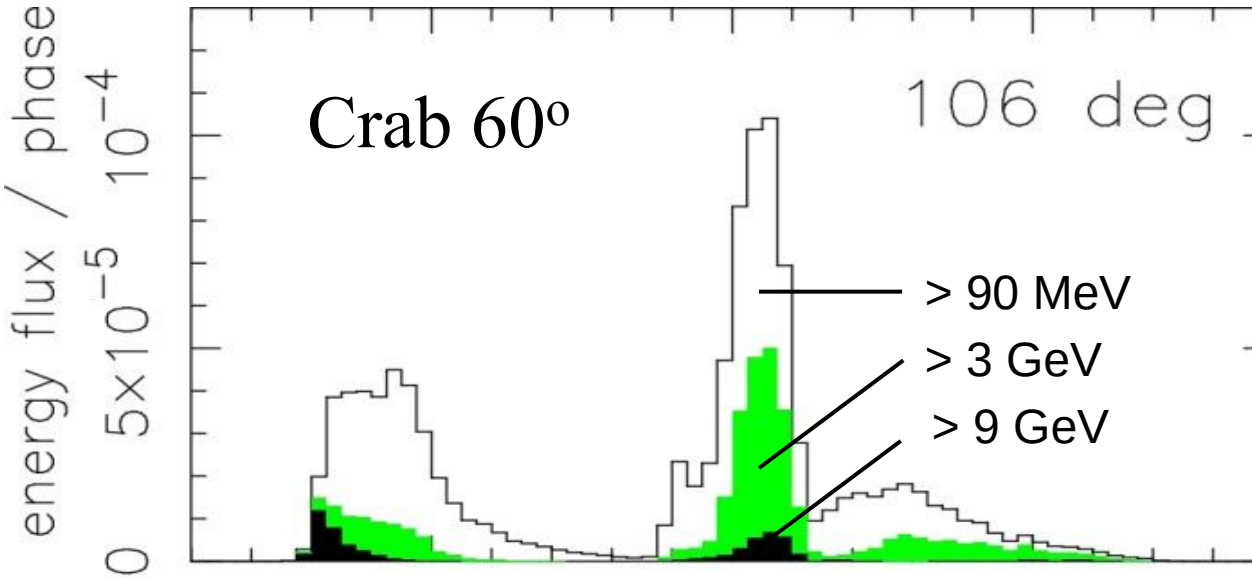

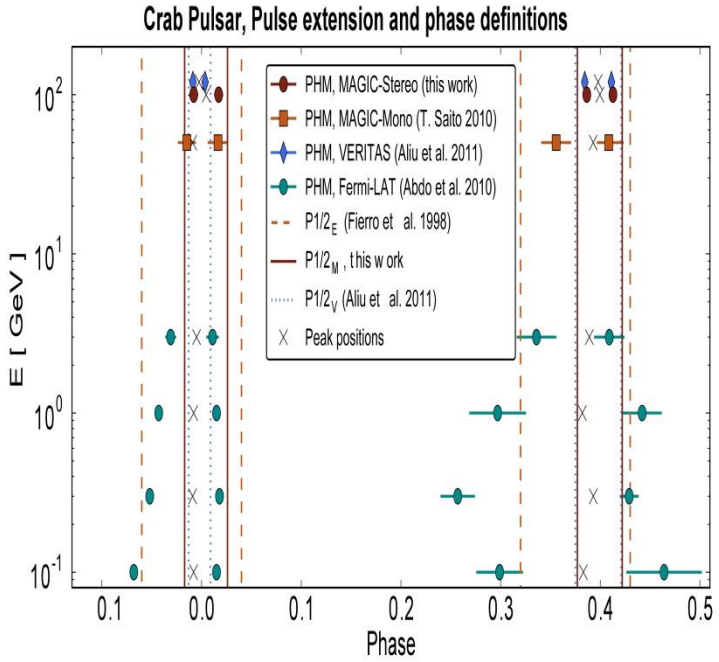

§7 ICS spectrum of the Crab pulsar

Phase-averaged spectrum

solid: primary (bef. absorption)
dashed: secondary (bef. absorption)
dotted: tertiary (bef. absorption)
green: all (after absorption)

Crab, α=60°

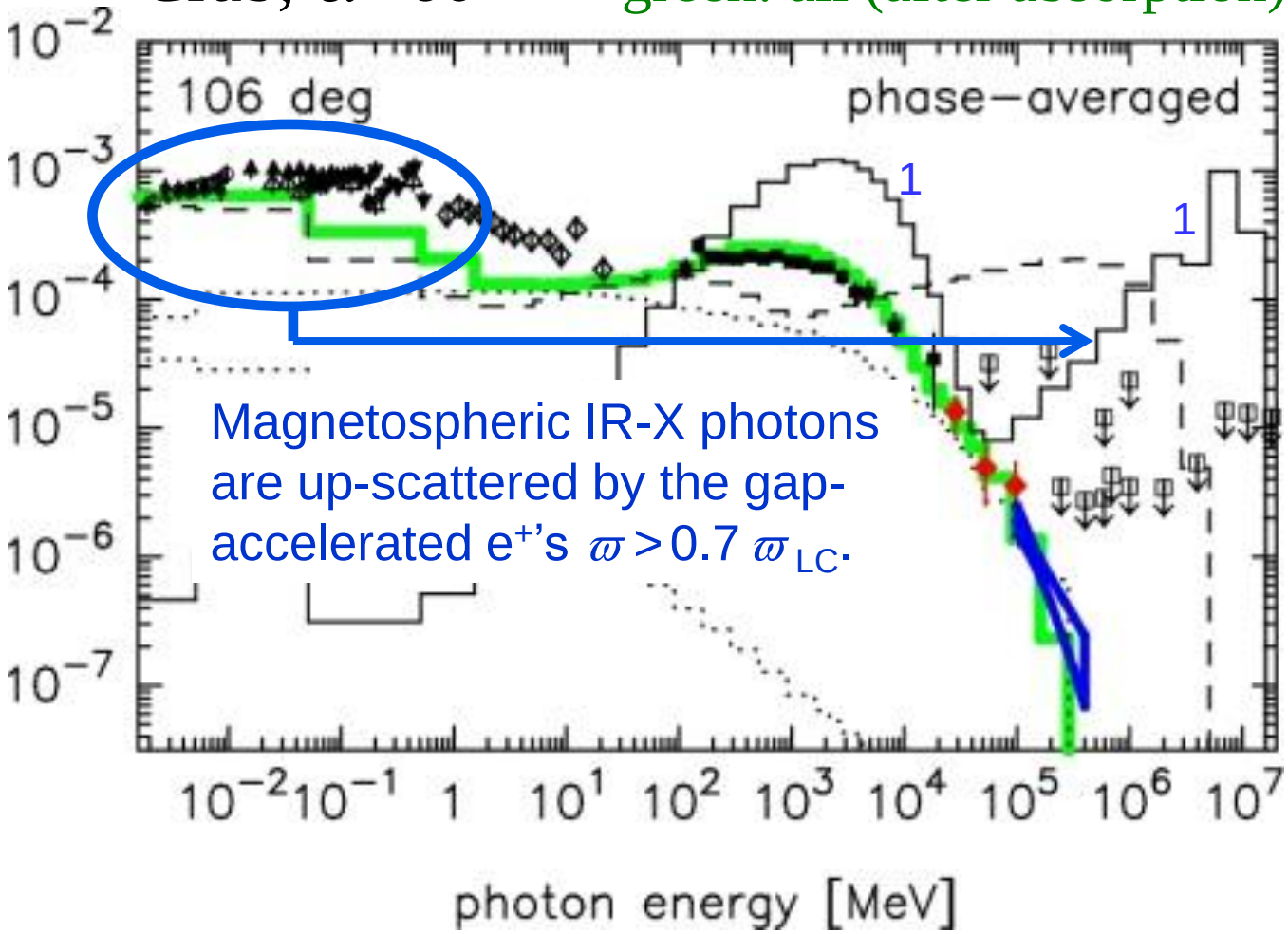

§7 ICS spectrum of the Crab pulsar

Phase-averaged spectrum

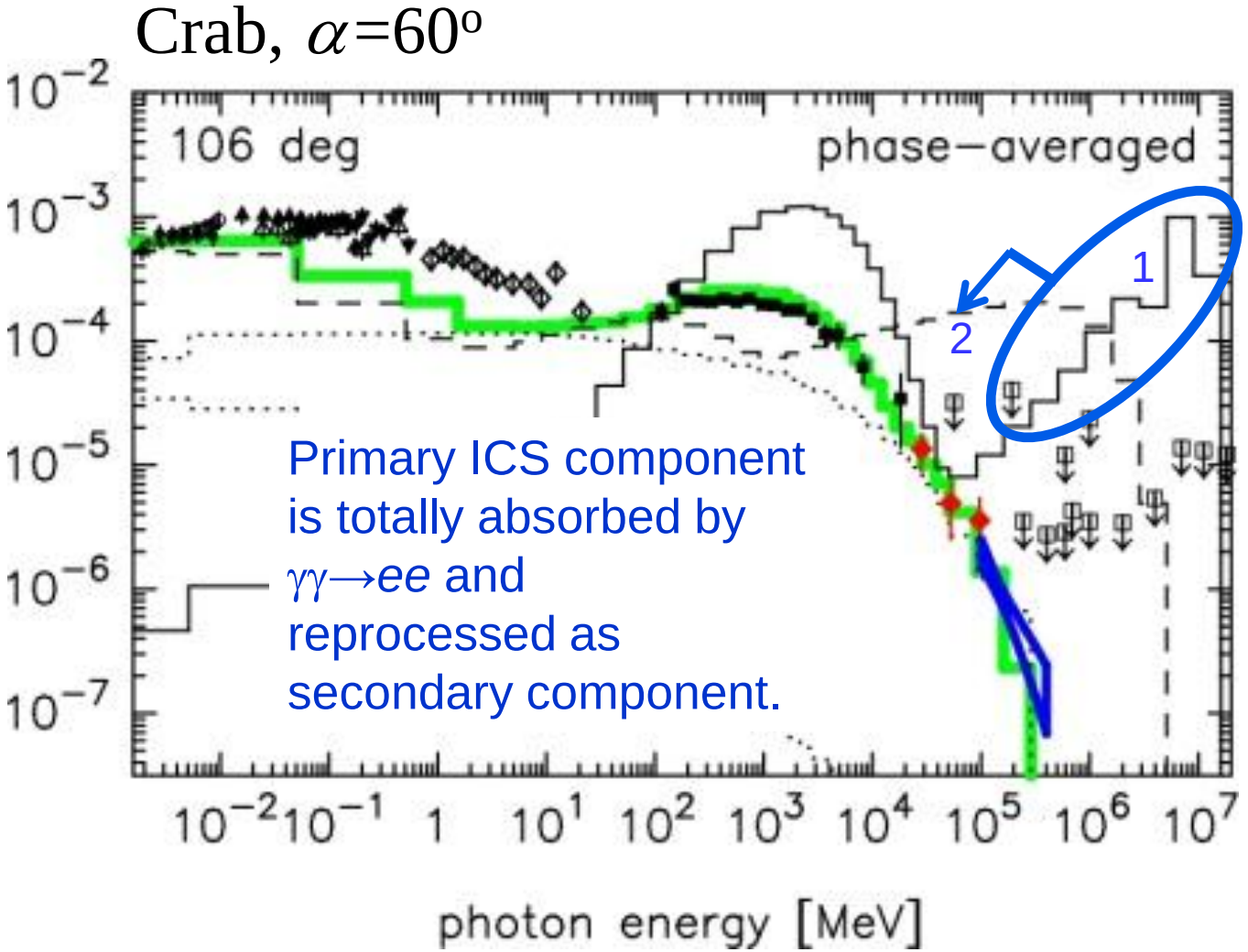

§7 ICS spectrum of the Crab pulsar

Phase-averaged spectrum

Crab, α=60°

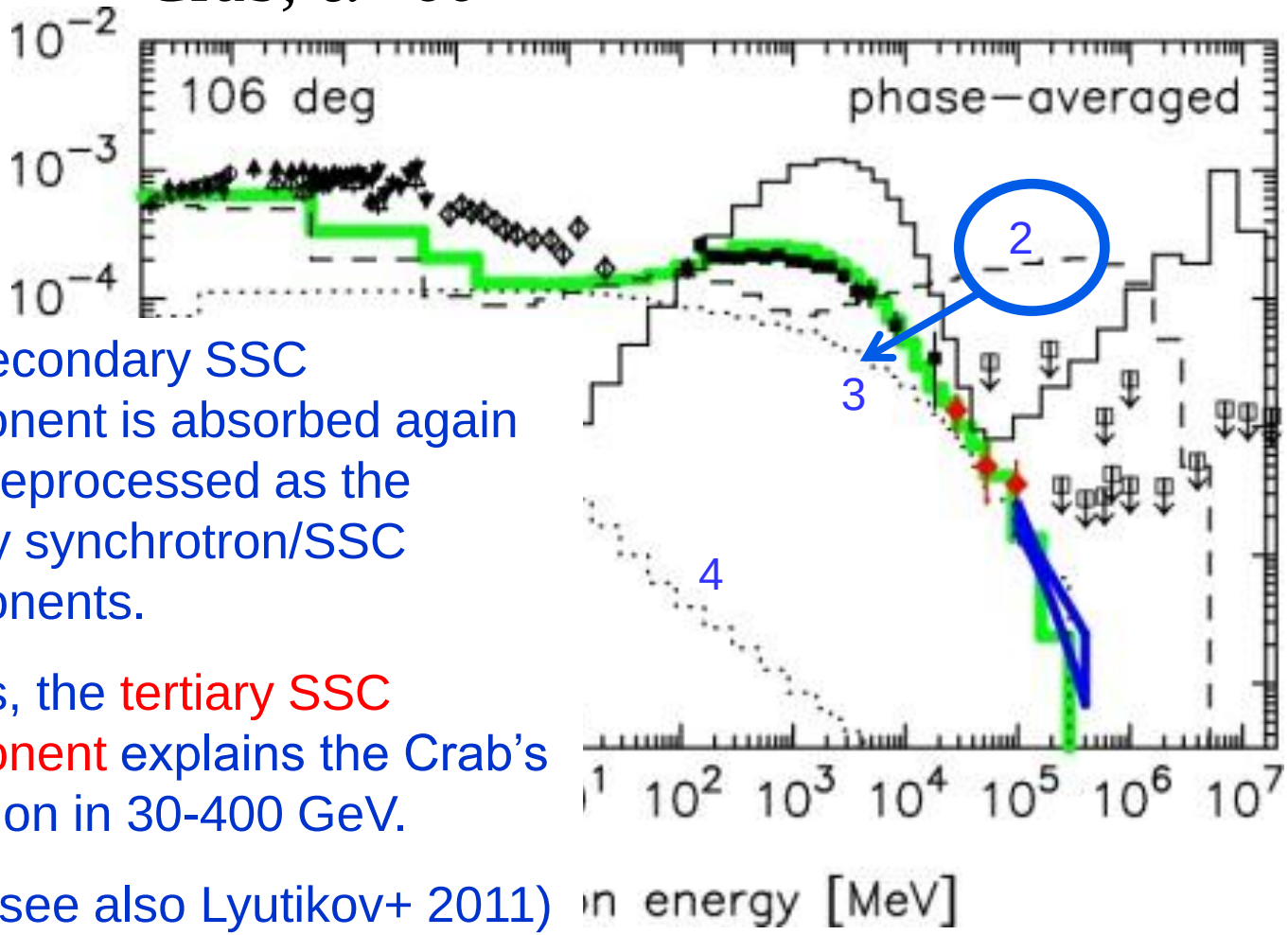

The secondary SSC component is absorbed again to be reprocessed as the tertiary synchrotron/SSC components.

That is, the tertiary SSC component explains the Crab's pulsation in 30-400 GeV.

(see also Lyutikov+ 2011)

§7 ICS spectrum of the Crab pulsar

Phase-resolved spectrum (in LAT-defined phase bins):

Crab, α=60^{o}

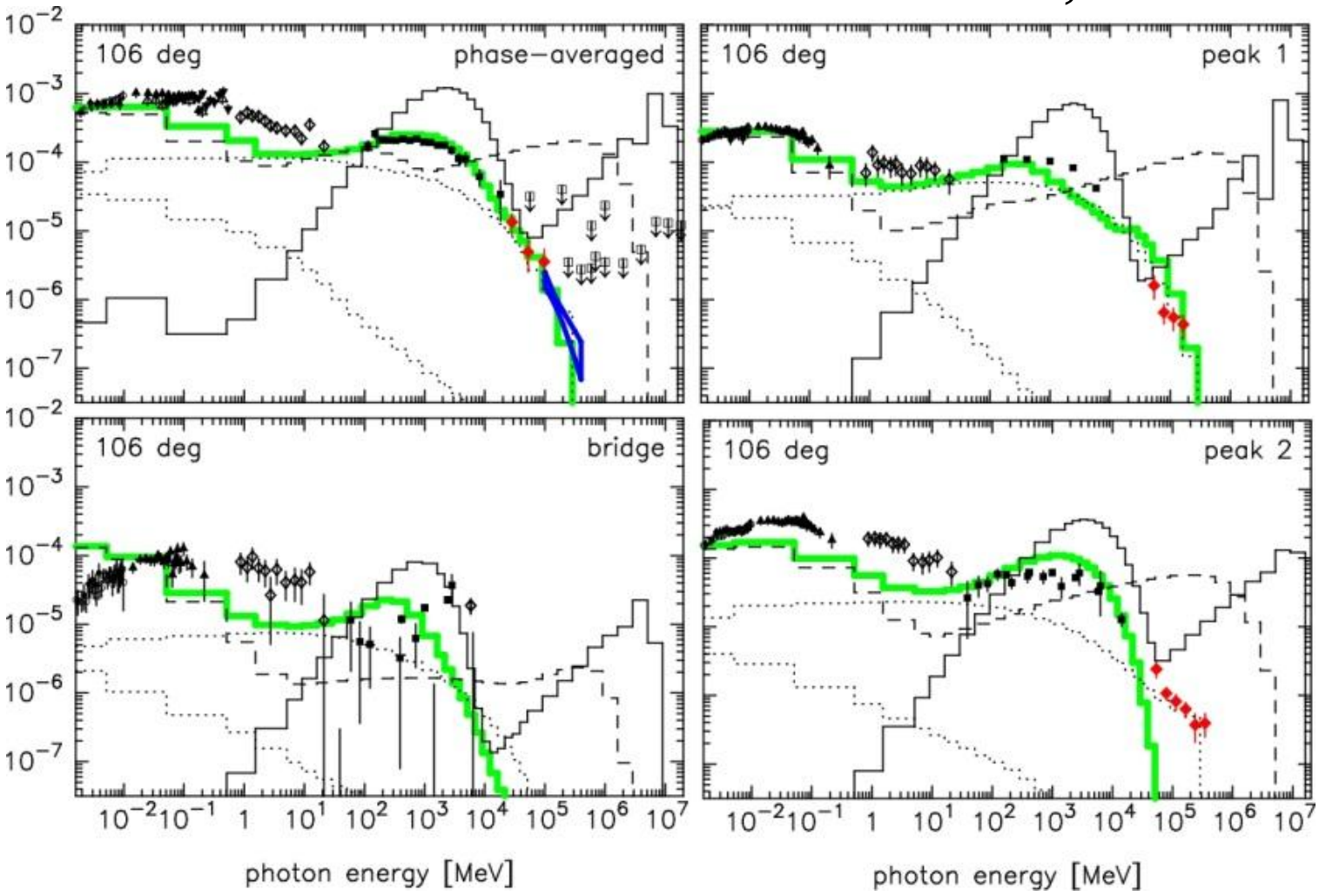

§7 ICS spectrum of the Crab pulsar

Phase-resolved spectrum (in LAT-defined phase bins):

Crab, α=60^o

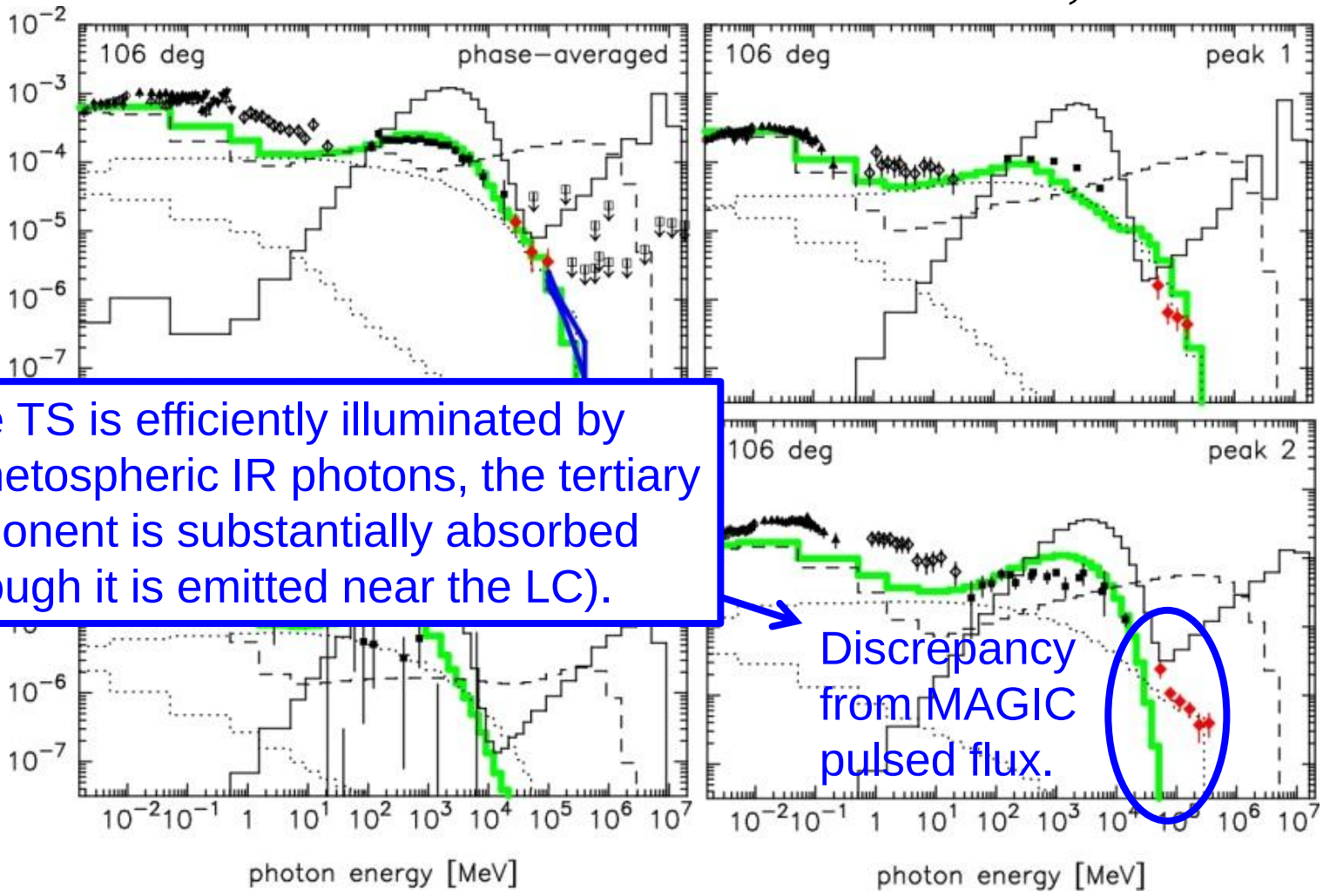

Since TS is efficiently illuminated by magnetospheric IR photons, the tertiary component is substantially absorbed (although it is emitted near the LC).

Discrepancy from MAGIC pulsed flux.

§7 ICS spectrum of the Crab pulsar

Phase-resolved spectrum (in LAT-defined phase bins):

Crab, α=60^o

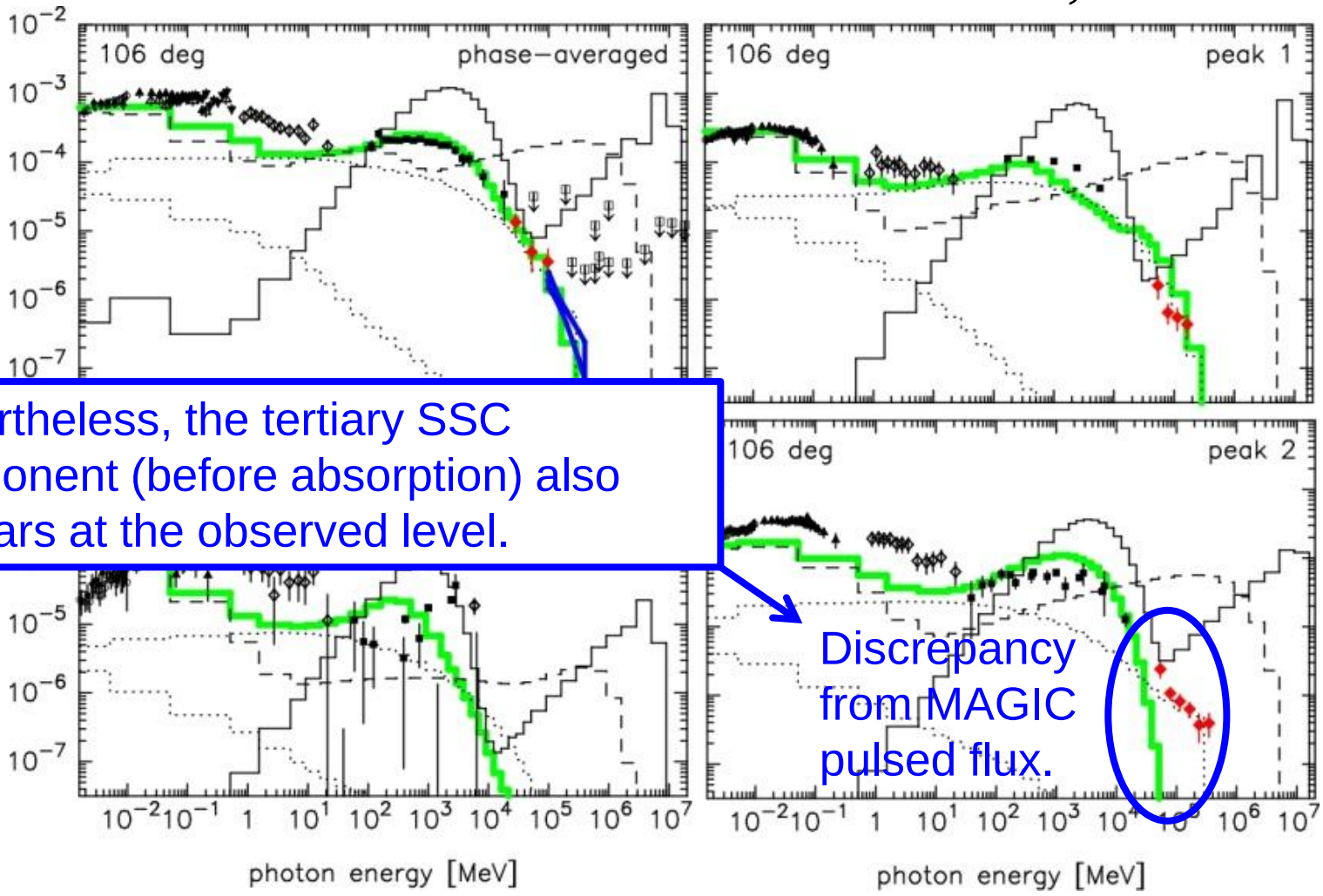

Nevertheless, the tertiary SSC component (before absorption) also appears at the observed level.

Discrepancy from MAGIC pulsed flux.

§7 ICS spectrum of the Crab pulsar

Two possibilities to get correct P2 spectrum:

(1)In TS, photons intensity concentrates in a small solid angle due to special relativistic effects. Thus, if I adopt finer grids for photon propagation directions, $\gamma\gamma \rightarrow ee$ optical depth may decrease in the TS, which helps the tertiary SSC component appear without absorption.

(2)The vacuum rotating dipole **B** field structure should be replaced with a more realistic one, e.g., force-free solution.

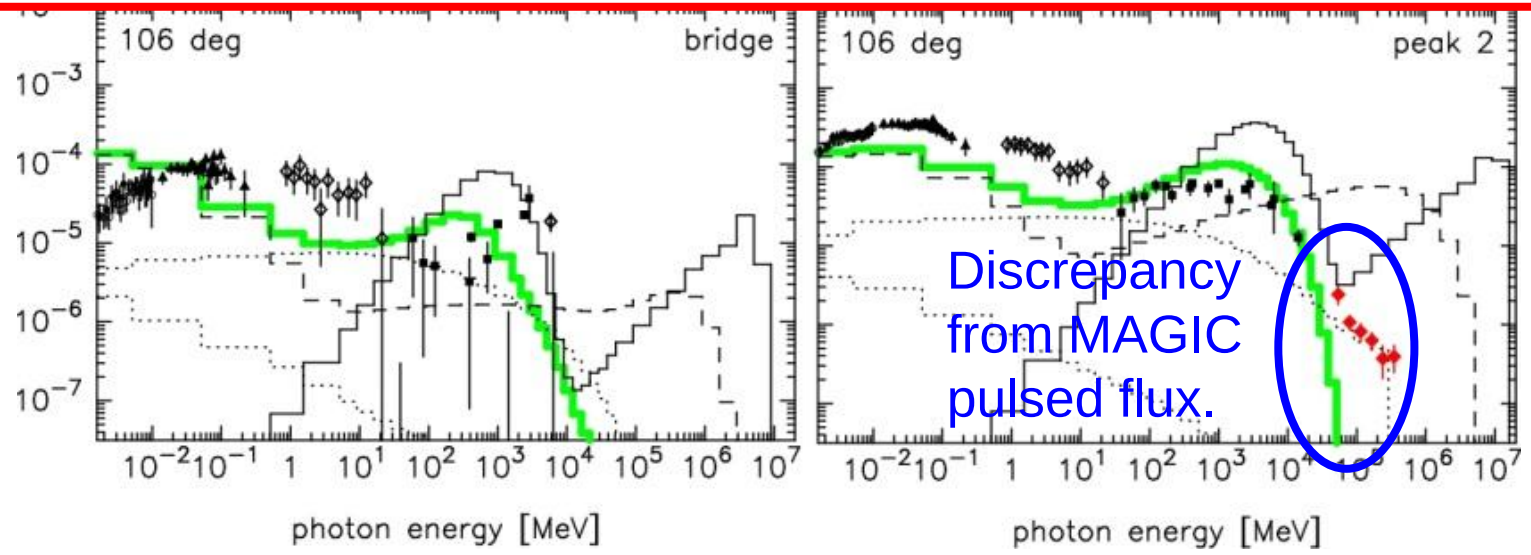

Summary

- We can now solve pulsed high-energy emissions from the set of Maxwell (div$\boldsymbol{E}=4\pi\rho$) and Boltzmann eqs., if we specify P, dP/dt, $\alpha_{\rm incl}$, $kT_{\rm NS}$. We no longer have to assume the gap geometry, $E_{\parallel}$, $e^{\pm}$ distribution functions.

- By SSC of secondary/tertiary pairs, Crab's total pulse spectrum shows a power-law-like shape.

- P2 exhibits harder curvature spectrum than P1, because actual particle path has greater curvature radius in the TS.

- Millisecond pulsar death line, which was obtained both analytically and numerically, is now being checked by Fermi groups.

Thank you.

§1 3-D Formalism of Gap Electrodynamics

Assuming $\partial_t+\Omega\partial_\phi=0$, we solve the $e^{\pm}$'s Boltzmann eqs.

$$\frac{\partial N_\pm}{\partial t}+\vec{v}\cdot\nabla N_\pm+\left(e\vec{E}_{\|}+\frac{\vec{v}}{c}\times\vec{B}\right)\cdot\frac{\partial N_\pm}{\partial \vec{p}}=S_{IC}+S_{SC}+\int\alpha_\nu d\nu\int\frac{I_\nu}{h\nu}d\omega$$

together with the radiative transfer equation,

$$\frac{dI_\nu}{dl}=-\alpha_\nu I_\nu+j_\nu$$

$N_\pm$: positronic/electronic spatial # density,
$E_{\|}$: mangnetic-field-aligned electric field,
$S_{\rm IC}$: ICS re-distribution function, $d\omega$: solid angle element,
I_ν: specific intensity, l : path length along the ray
α_ν: absorption coefficient, j_ν: emission coefficient

§3 Spectral Hardening in the Trailing Peak